Algorithmic aspects and finite element solutions for advanced phase field approach to martensitic phase transformation under large strains

3 authors:

Hamed Babaei
Iowa State University
8 PUBLICATIONS **113** CITATIONS

SEE PROFILE

Anup Basak
Indian Institute of Technology Tirupati
17 PUBLICATIONS **50** CITATIONS

SEE PROFILE

Valery I. Levitas
Iowa State University
315 PUBLICATIONS **6,233** CITATIONS

SEE PROFILE

Some of the authors of this publication are also working on these related projects:

Study of energetic material (azide) under high pressure View project

Mapping and Manipulating Phase Transitions View project

Algorithmic aspects and finite element solutions for advanced phase field approach to martensitic phase transformation under large strains

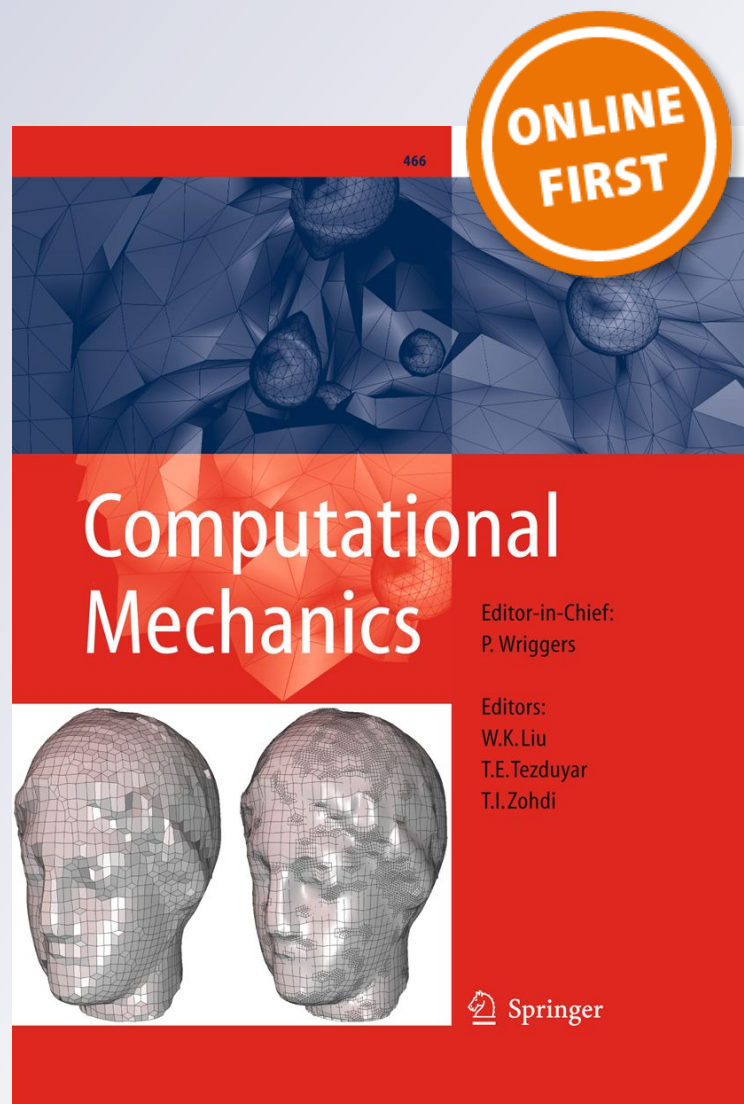## Hamed Babaei, Anup Basak & Valery I. Levitas

ONLINE FIRST

466

Computational Mechanics

Editor-in-Chief:
P. Wriggers

Editors:
W.K. Liu
T.E.Tezduyar
T.I. Zohdi

Springer

Springer

Springer

ORIGINAL PAPER

Algorithmic aspects and finite element solutions for advanced phase field approach to martensitic phase transformation under large strains

Hamed Babaei[1] · Anup Basak[1] · Valery I. Levitas[2]

Abstract
A new problem formulation and numerical algorithm for an advanced phase-field approach (PFA) to martensitic phase transformation (PT) are presented. Finite elastic and transformational strains are considered using a fully geometrically-nonlinear formulation, which includes different anisotropic elastic properties of phases. The requirements for the thermodynamic potentials and transformation deformation gradient tensor are advanced to reproduce crystal lattice instability conditions under a general stress tensor obtained by molecular dynamics (MD) simulations. The PFA parameters are calibrated, in particular, based on the results of MD simulations for PTs between semiconducting Si I and metallic Si II phases under complex action of all six components of the stress tensor (Levitas et al. in Phys Rev Lett 118:025701, 2017a; Phys Rev B 96:054118, 2017b). The independence of the PFA instability conditions of the prescribed stress measure is demonstrated numerically for the initiation of the PT. However, it is observed that the PT cannot be completed unless the stress exceeds the stress peak points that depend on which stress measure is prescribed. Various 3D problems on lattice instability and following nanostructure evolution in single-crystal Si are solved. The effect of stress hysteresis on the nanostructure evolution is studied through analysis of the local driving force and stress fields. It is demonstrated that variation of internal stress fields due to differing boundary conditions may lead to completely different PT mechanisms.

1 Introduction

The martensitic PTs are widely modeled using PFA [1,6,18, 30,31,38,45,50]. Within the PFA framework, the process of PT is characterized by an internal variable or order parameter η, being $\eta = 0$ for the parent phase P_0 and $\eta = 1$ for the product phase P_1. The order parameter changes gradually within a diffuse interface between the bulk phases. In some theories, the order parameter [1,6,18,45] does not have a specific physical meaning. However, other theories [4,7,8,14,44] have used some components of the strain tensor as the order parameter. We will only focus on the first theories because

there are some problems with the strain-tensor-based order parameters mentioned in [30,31].

One of the most important aspects of developing a successful PFA is the formulation of local thermodynamic potentials that properly interpolate the material properties during the transformation process and provide appropriate energetic barriers between the parent and product phases. Some theories [1,6,8,14,18,44,45] only consider two requirements to be satisfied by the potentials: first, that the number of local extrema of the potentials is equal to the number of phases including martensitic variants; second, that the energy is invariant with respect to the exchange of equivalent symmetry-related martensitic variants. Because these theories do not thermodynamically constrain the order parameter $\eta = 1$ for the product phase P_1, the thermodynamic equilibrium value of the order parameter for P_1 artificially depends on the stress tensor and temperature, as well as all material properties of the product phase. Additional requirements have been proposed in [30,31,34] and will be discussed here resulting in two constraints, Eqs. (15) and (19) for any interpolation function in the local potential. These requirements

✉ Valery I. Levitas
vlevitas@iastate.edu

[1] Department of Aerospace Engineering, Iowa State University, Ames, IA 50011, USA

[2] Departments of Aerospace Engineering, Mechanical Engineering, and Material Science & Engineering, Iowa State University, Ames, IA 50011, USA

lead to both fourth degree (2–3–4) and sixth degree (2–4–6) potentials in terms of the transformation strain-related order parameter; the potentials reproduce the desirable stress–strain curves and material properties. The mentioned theory was generalized to large strain formulation in [22,35], where the transformation deformation gradient was interpolated between the parent and product phases. Besides, interfacial stresses for martensitic PTs were introduced in the small strain formulation in [23–25,28] and were generalized for large strains in [26] for isotropic interfacial energy and in [33] for anisotropic interfacial energy.

One more condition formulated in [22,30,31,34] was that the criteria for the initiation of the direct and reverse PTs should follow from the crystal lattice instability conditions obtained by experimentation or atomistic simulations. The lattice instability conditions are highly essential when studying barrierless nucleation during martensitic PTs for thermally-induced transformations [40–42]. These conditions are even more crucial for explaining plastic strain-induced PTs under high pressure when PT pressure is drastically reduced even by one order of magnitude through superposing plastic shear [5,17,32]. This reduction was rationalized by considering barrierless nucleation under evolving dislocation pileup, initially analytically in [20,21] and, later using the phase field approach in [15,16,29].

On one hand, the PFA instability criteria operate with the second derivatives of the interpolation functions [22,30,31, 34]; on the other hand, the constraints on the interpolation functions in the previous theories were limited to the values of the functions and their first derivatives at $\eta = 0$ and $\eta = 1$. Therefore, the previous theories fail to reproduce the actual lattice instability conditions because they cannot control the second derivatives of interpolation functions. Therefore, to reproduce the actual instability conditions, the interpolation functions in PFA need to be advanced.

Recently, the lattice instability conditions for cubic-tetragonal PTs between semiconducting Si I and metallic Si II were obtained using MD simulations for complex compression-tension and shear loadings [36,37]. It was demonstrated that only modified transformation work of the components of stress tensor which are normal to the cubic faces of Si I contribute to the instability conditions. Because the transformation strain has no shear components, the shear stresses do not directly contribute to the instability conditions. Besides, the instability conditions were two linear expressions in terms of normal stress components. Therefore, the instability conditions can be presented as two intersecting planes in 3D stress space. These two planes were not parallel, so they could not be described by the 2–3–4 or 2–4–6 thermodynamic potentials, which produce parallel direct and reverse instability planes. In addition, these two planes coincide after intersection in [36,37]. Thus, new conditions must be introduced to make the PFA instability criteria consistent with the lattice instability conditions obtained by atomistic simulations. These conditions were introduced in [2,27] and is implemented in this work.

This paper aims to develop the algorithmic aspects of the solution of coupled large-strain mechanics and Ginzburg–Landau equations for an advanced phase field model which reproduce instability conditions obtained by atomistic simulations. We illustrate the main features through finite element solutions for mechanically-induced PTs and nanostructure evolution. In particular, we will focus on cubic $\leftrightarrow$ tetragonal PTs between diamond cubic low-pressure phase Si I and β tin high-pressure phase Si II. Large transformational and finite elastic deformations are involved in solution under complex triaxial loading and corresponding nanostructure evolution.

Silicon crystals are widely used in the field of precision instruments for micro-electro-mechanical systems (MEMS), which include piezoelectric materials, resonators, etc. Besides, interest in the usage of nanostructured crystals such as thin films, rods, wires and balls for new applications, such as nanowires for lithium batteries, has increased. Under pressure and contact loading Si undergoes multiple PTs. We will focus on PTs between semiconducting Si I and metallic Si II phases. Thus, Si I $\rightarrow$ Si II PT occurs at hydrostatic pressure or under indentation in the range of pressures or contact stresses of 9–12 GPa [9]. Such a local load may appear under contacting or scratching MEMS elements, during Si wafer processing, and during fabrication of devices. Also, PT from brittle and hard semiconducting Si I to softer and weaker metallic Si II leads to a ductile regime of machining of Si [43]. This is why there is extended literature for the study of PTs in Si under different hydrostatic and nonhydrostatic loadings; see review in [9]. Very large and anisotropic transformation strain for this transition and ways of accommodating it without twinning leads to additional interest in the mechanical community but imposes additional computational challenges. Studying these transformations is important for the understanding of PTs with large transformation strain in other materials, such as graphite-diamond, graphite-like to diamond-like born nitride, and geophysical materials. We consider PTs Si I $\leftrightarrow$ Si II here because these are the only transformations for which the transformation criteria under the stress tensor are obtained via molecular dynamics (MD) simulations [36,37] and density functional theory (DFT) simulations [49]. We consider uniaxial and triaxial loading by normal-to-cubic-faces stresses as the simplest macro-homogeneous loading. Unfortunately, we cannot compare our results for defect-free crystal with experimental data because, e.g. for compression of micro- [47] and nano-pillars [10] of real crystals, dislocation motion and other PTs occur before the required stresses are reached. Indentation and experiments in diamond anvils, where PT Si I $\rightarrow$ Si II is observed, do not allow a microstructure evolution to be found.

In this paper, we focus on three fundamental aspects of PTs in Si crystals within the phase-field approach. First, we provide a new understanding of the crystal lattice instability conditions and show that the traditional expression of crystal lattice instability merely in terms of the Cauchy stress measure may not hold true for all loadings and boundary conditions. Second, we show how the difference between the reverse instability stresses, i.e. stress hysteresis, affects the nanostructure evolution. Third, the effects of internal stresses due to interfaces are investigated when a periodic BC is compared with a free-stress BC in the thickness direction of a thin plate.

In Sect. 2, the complete systems of equations for PFA to martensitic PTs for the large-strain kinematic model are presented. A single martensitic variant is considered, similar to that which was observed in atomistic simulations in [36,37] and described in theory by [2,27]. The kinematic model is based on interpolation of the transformation strain tensor. Besides, the new advances regarding the requirements for the interpolation functions are discussed in this section. These advancements lead to new interpolation functions for transformation strain and the elastic constants. The resultant PFA instability conditions, which have been calibrated with atomistic simulations are presented. The finite element algorithm and weak forms of the Ginzburg–Landau and equilibrium equations are presented in Sect. 3. A non-monolithic strategy for solving the coupled mechanics and phase field equations is adopted. While solving the equilibrium equations, the order parameter is assumed to be fixed in all iterations, and while solving the Ginzburg–Landau equation, the total deformation gradient is assumed to be fixed in all iterations. The simulation results are discussed in Sect. 4. First, it is numerically demonstrated that on one hand, the initiation of the PT, which is determined by our PFA instability criteria is independent of which stress measure is prescribed; on the other hand, the PT will not be completed unless the stress exceeds the stress peak point, which depends on the prescribed stress measure. Second, the effect of stress hysteresis in the model on nanostructure evolution is studied through analysis of the order parameter, driving force, and stress fields. Third, the effect of the boundary conditions in the thickness direction, which leads to a completely different interfacial stress in this direction and in turn changes the mechanism of PT, is studied.

Vectors and tensors are designated with boldface symbols. We designate contractions of tensors $\boldsymbol{A} = \{A_{ij}\}$ and $\boldsymbol{B} = \{B_{ji}\}$ over one and two indices as $\boldsymbol{A}\cdot\boldsymbol{B} = \{A_{ij} B_{jk}\}$ and $\boldsymbol{A}:\boldsymbol{B} = A_{ij} B_{ji}$. The transpose of $\boldsymbol{A}$ is $\boldsymbol{A}^T$, the symmetric part of $\boldsymbol{A}$ is $sym(\boldsymbol{A})$ and $\boldsymbol{I}$ is the unit tensor; ∇_0 is the gradient operator with respect to the undeformed state.

2 Complete system of equations

Here, the complete system of equations for the general phase-field theory, developed in [27] (which takes into account the lattice instability conditions obtained by atomistic simulations) is simplified and specified. First, the interfacial stresses are neglected by presenting the gradient part of free energy in the reference configuration. Second, the simplest quadratic form in terms of Lagrangian strain is accepted for the elastic energy. Third, only the diagonal components of the transformation strain are interpolated, neglecting the small effect of shear stresses on the crystal lattice instability for cubic-to-tetragonal PTs. Although the formulation presented here can be used for any stress-induced martensitic PT, the calibration of the PT criteria with atomistic simulations is performed specifically for the cubic-to-tetragonal Si I ↔ Si II PTs. At the same time, our algorithmic part does not use all of these simplifications and is valid for the general theory presented in [27].

2.1 Kinematics

The motion of an elastic body undergoing PTs can be expressed by a continuous function $\boldsymbol{r} = \boldsymbol{r}(\boldsymbol{r}_0, t)$, where $\boldsymbol{r}_0$ and $\boldsymbol{r}$ are the positions of points in the undeformed Ω_0 and the deformed Ω configurations, respectively; t is the time. The stress-free intermediate configuration is denoted by Ω_t. The external boundary in Ω_0 is denoted by S_0, which consists of the traction boundary (Neumann boundary) S_{0T}, the displacement boundary (Dirichlet boundary) S_{0u}, and the periodic displacement boundary S_{0u}^P, i.e. $S_0 = S_{0u} \cup S_{0T} \cup S_{0u}^P$. For the phase field problem, the boundary S_0 consists of either the Neumann boundary $S_{0\eta}^N$, the Dirichlet boundary $S_{0\eta}^D$, the periodic boundary $S_{0\eta}^P$, or a combination any two or all three kinds of boundaries.

The multiplicative decomposition of the deformation gradient into the elastic part and a symmetric, rotation-free transformational part is

$$\boldsymbol{F} := \nabla_0 \boldsymbol{r} = \boldsymbol{F}_e \cdot \boldsymbol{U}_t; \qquad \boldsymbol{U}_t = \boldsymbol{U}_t^T. \tag{1}$$

In the intermediate configuration Ω_t, obtained by the transformation deformation $\boldsymbol{U}_t$, the crystal lattice represents the lattice of the stress-free product phase or intermediate phase along the transformation path from the lattice of Si I to that of Si II. This configuration is obtained through the release of elastic stresses down to zero from the actual configuration Ω.

We need the Jacobian determinants, describing the ratios of the volumes in the different configurations:

$$J = \frac{dV}{dV_0} = det\,\boldsymbol{F}; \quad J_e = \frac{dV}{dV_t} = det\,\boldsymbol{F}_e;$$

$$J_t = \frac{dV_t}{dV_0} = det\boldsymbol{U}_t \qquad J = J_e J_t. \tag{2}$$

The Lagrangian total, elastic, and transformation strains are given respectively by

$$\boldsymbol{E} = \frac{1}{2}(\boldsymbol{F}^t \cdot \boldsymbol{F} - \boldsymbol{I}); \quad \boldsymbol{E}_e = \frac{1}{2}(\boldsymbol{F}_e^t \cdot \boldsymbol{F}_e - \boldsymbol{I});$$
$$\boldsymbol{E}_t = \frac{1}{2}(\boldsymbol{U}_t \cdot \boldsymbol{U}_t - \boldsymbol{I}); \qquad \boldsymbol{E} = \boldsymbol{U}_t \cdot \boldsymbol{E}_e \cdot \boldsymbol{U}_t + \boldsymbol{E}_t. \tag{3}$$

2.2 Dissipation rate, equations for stresses, and Ginzburg–Landau equation

With the help of the first and second laws of thermodynamics, along with acceptance of $\psi = \bar{\psi}(\boldsymbol{F}, \eta, \theta, \nabla_0 \eta)$ as the Helmholtz free energy per unit volume, we can derive the expression for the dissipation rate per unit volume D, as follows:

$$D = X\dot{\eta} \geq 0; \qquad \rho_0 X := -\rho_0 \frac{\partial \bar{\psi}}{\partial \eta} + \nabla_0 \cdot \left(\rho_0 \frac{\partial \bar{\psi}}{\partial \nabla_0 \eta}\right), \tag{4}$$

where X is the thermodynamic driving force per unit volume for change in the order parameter η (i.e. for PT) and θ is the temperature. Through the same thermodynamic procedure, by assuming that the dissipation rate is independent of the elastic deformation rate and temperature rate, we can also find the expressions for the first Piola–Kirchhoff stress $\boldsymbol{P}$ (and transform it to the true Cauchy stress $\boldsymbol{\sigma}$) and the entropy s:

$$\boldsymbol{P} = \rho_0 \frac{\partial \bar{\psi}}{\partial \boldsymbol{F}}; \qquad \boldsymbol{\sigma} := J^{-1} \boldsymbol{P} \cdot \boldsymbol{F}^t = \rho \frac{\partial \bar{\psi}}{\partial \boldsymbol{F}} \cdot \boldsymbol{F}^t; \qquad s = -\frac{\partial \bar{\psi}}{\partial \theta}, \tag{5}$$

The viscous stresses are neglected for compactness.

Accepting a linear relationship between the rate of change of the order parameter $\dot{\eta}$ and the conjugate generalized thermodynamic force X, we can obtain the generalized Ginzburg–Landau equation, which describes the evolution of the martensitic nanostructure as

$$\dot{\eta} = LX = L\left(-\frac{\partial \bar{\psi}}{\partial \eta}\bigg|_{\boldsymbol{E}} + \nabla_0 \cdot \left(\frac{\partial \bar{\psi}}{\partial \nabla_0 \eta}\right)\right), \tag{6}$$

where $L \geq 0$ is the kinetic coefficient. Atomistic simulations in [36,37] and [49] were performed at 1 K and 0 K, respectively. Therefore, thermal fluctuations are neglected and the Langevin noise is not included in the Ginzburg–Landau equation.

The Helmholtz free energy per unit volume in the reference configuration can be written as the sum of local, ψ^l, and gradient, ψ^∇, parts:

$$\bar{\psi}(\boldsymbol{F}, \eta, \theta, \nabla_0 \eta) = \psi^l(\boldsymbol{E}_e, \eta, \theta) + \psi^\nabla(\nabla_0 \eta)$$
$$= J_t \psi^e(\boldsymbol{E}_e) + \psi^\theta + \psi^\nabla, \tag{7}$$

where ψ^e is the elastic energy per unit volume in the intermediate configuration Ω_t, which is the reference configuration for the elasticity rule. The thermal part of the free energy includes the energy barrier between phases as well as the thermal driving force for phase transformation and is accepted in one of the known forms:

$$\psi^\theta = A\eta^2(1 - \eta)^2 + \Delta\psi^\theta(3\eta^2 - 2\eta^3). \tag{8}$$

Here A is the magnitude of the double-well barrier between the parent phase P_0 and the product phase P_1 and $\Delta\psi^\theta$ is the difference between the thermal free energy of P_1 and P_0. The gradient part of the free energy penalizes interfaces and is expressed as

$$\psi^\nabla = \frac{\beta}{2}|\nabla_0 \eta|^2, \tag{9}$$

where $\beta \geq 0$ is a coefficient. Using Eqs. (1), (2), and (7) in Eq. (5) we rewrite the first Piola–Kirchhoff and the Cauchy stress tensors as

$$\boldsymbol{P} = J_t \boldsymbol{F}_e \cdot \hat{\boldsymbol{S}} \cdot \boldsymbol{U}_t^{-1};$$
$$\boldsymbol{\sigma} = J_e^{-1} \boldsymbol{F}_e \cdot \hat{\boldsymbol{S}} \cdot \boldsymbol{F}_e^T, \quad \text{where } \hat{\boldsymbol{S}} = \frac{\partial \psi^e(\boldsymbol{E}_e)}{\partial \boldsymbol{E}_e}. \tag{10}$$

Using the standard relation between the second Piola–Kirchhoff stress $\boldsymbol{S}$ and the two other stresses $\boldsymbol{P} = \boldsymbol{F} \cdot \boldsymbol{S} = J\boldsymbol{\sigma} \cdot \boldsymbol{F}^{-T}$ we obtain

$$\boldsymbol{S} = J_t \boldsymbol{U}_t^{-1} \cdot \hat{\boldsymbol{S}} \cdot \boldsymbol{U}_t^{-1}. \tag{11}$$

Substituting the free energy Eqs. (7) into (6) leads to a more explicit form of the Ginzburg–Landau equation in the reference configuration

$$\dot{\eta} = LX$$
$$= L\left(\boldsymbol{P}^T \cdot \boldsymbol{F}_e : \frac{\partial \boldsymbol{U}_t}{\partial \eta}\right.$$
$$\left. - J_t \frac{\partial \psi^e}{\partial \eta}\bigg|_{\boldsymbol{E}_e} - J_t \psi^e \boldsymbol{U}_t^{-1} : \frac{\partial \boldsymbol{U}_t}{\partial \eta} - \frac{\partial \psi^\theta}{\partial \eta} + \beta\nabla_0^2 \eta\right). \tag{12}$$

There are two solution variables in the PFA, namely the order parameter and the displacement. The former is calculated by the Ginzburg–Landau equation and the latter by the mechanical equilibrium equation in the reference configuration, which is known as

$$\nabla_0 \cdot \boldsymbol{P} = \boldsymbol{0}. \tag{13}$$

2.3 Conditions for interpolation functions

One of the most important problems in any phase field theory is how to describe the dependence of all material properties that contribute the free energy $\bar{\psi}$, as well as the transformational deformation gradient $\boldsymbol{U}_t$ on the order parameter η. Here, we will enumerate the main conditions that should be satisfied in this regard.

It is reasonable to express any material property M (such as energy, entropy, elastic moduli, thermal expansion, etc.) in the form

$$M(\eta, \theta) = M_0(\theta) + (M_1(\theta) - M_0(\theta))\varphi_m(\eta), \quad (14)$$

where M_0 and M_1 are values of the property for the parent phase P_0 (for which $\eta = 0$) and the product phase P_1 (for which $\eta = 1$), respectively; $\varphi_m(\eta)$ is the interpolation function that meets the evident constraints

$$\varphi_m(0) = 0, \qquad \varphi_m(1) = 1. \quad (15)$$

Because the order parameter should not evolve further after reaching the homogeneous equilibrium bulk phases, P_0 and P_1, the thermodynamic equilibrium conditions for homogeneous states (i.e., $\nabla_0^2 \eta = 0$) should be satisfied by the order parameter values for bulks $\hat{\eta}$ (i.e. $\eta = 0$ and $\eta = 1$):

$$\rho_0 X = \boldsymbol{P}^t \cdot \boldsymbol{F}_e : \frac{d\boldsymbol{U}_t(\hat{\eta})}{d\eta} - J_t \frac{\partial \psi^e(\boldsymbol{E}_e, \theta, \hat{\eta})}{\partial \eta}\bigg|_{\boldsymbol{F}_e} - J_t \psi^e(\boldsymbol{E}_e, \theta, \hat{\eta})\boldsymbol{U}_t^{-1} : \frac{d\boldsymbol{U}_t(\hat{\eta})}{d\eta}$$
$$- J\rho_0 \frac{\partial \breve{\psi}^\theta(\theta, \hat{\eta})}{\partial \eta} - \rho_0 \frac{\partial \breve{\psi}^\theta(\theta, \hat{\eta})}{\partial \eta} = 0 \quad (16)$$

for any stress $\boldsymbol{P}$, temperature θ, and corresponding elastic deformation gradient $\boldsymbol{F}_e$. Equation (16) can be expressed in a compact form as

$$\rho_0 X = \boldsymbol{P}^T \cdot \boldsymbol{F}_e : \frac{d\boldsymbol{U}_t(\hat{\eta})}{d\eta} - \rho_0 \frac{\partial \psi^l(\boldsymbol{E}_e, \theta, \hat{\eta})}{\partial \eta} = 0. \quad (17)$$

Due to the independence of $\boldsymbol{U}_t$ and ψ^l, Eq. (17) splits into two sets of equations:

$$\frac{d\boldsymbol{U}_t(\hat{\eta})}{d\eta} = 0; \qquad \frac{\partial \psi^l(\boldsymbol{E}_e, \theta, \hat{\eta})}{\partial \eta} = 0. \quad (18)$$

Therefore, Eq. (18) results in the second condition to be satisfied by the interpolation function for the transformation deformation gradient and any material property which participates in ψ^l as follows

$$\frac{d\varphi_m(0)}{d\eta} = \frac{d\varphi_m(1)}{d\eta} = 0. \quad (19)$$

The third condition for interpolation functions is related to the instability criteria. Specifically, the PFA criteria for thermodynamic instability of equilibrium phases should coincide with the actual lattice instability conditions obtained using atomistic simulations or experiments.

By definition, if a spontaneous deviation of the order parameter $\Delta\eta$ from the thermodynamic equilibrium values $\hat{\eta} = 0$ or 1 is thermodynamically admissible under the prescribed boundary conditions, the equilibrium is unstable; this results in the general criterion for the instability of the equilibrium of phase $\hat{\eta}$ [22,27]:

$$\frac{\partial X(\boldsymbol{P}, \boldsymbol{F}_e, \eta)}{\partial \eta} = \boldsymbol{P}^T \cdot \boldsymbol{F}_e : \frac{\partial^2 \boldsymbol{U}_t}{\partial \eta^2} - J_t \frac{\partial^2 \psi^e}{\partial \eta^2}\bigg|_{\boldsymbol{E}_e}$$
$$- J_t \psi^e \boldsymbol{U}_t^{-1} : \frac{\partial^2 \boldsymbol{U}_t}{\partial \eta^2} - \frac{\partial^2 \psi^\theta}{\partial \eta^2} \geq 0, \quad \eta = \hat{\eta}. \quad (20)$$

The lattice instability conditions for cubic to tetragonal Si I $\leftrightarrow$ Si II PTs were obtained via MD simulations for various combinations of all six components of the Cauchy stress tensor in [36,37]. In 3D stress σ_i space, with the loading by stress σ_3 under fixed σ_1 and σ_2, all points for direct and reverse instability stresses have been located close to two intersecting planes:

$$P_0 \rightarrow P_1 :$$
$$\begin{cases} 0.36(\sigma_1 + \sigma_2) - \sigma_3 \geq 12.29 \text{ GPa} \quad if \quad -\sigma_3 \geq 6.23 \text{ GPa} \\ 0.19(\sigma_1 + \sigma_2) - \sigma_3 \geq 9.45 \text{ GPa} \quad otherwise \end{cases}$$
$$P_1 \rightarrow P_0 : \qquad 0.19(\sigma_1 + \sigma_2) - \sigma_3 \leq 9.45 \text{ GPa}. \quad (21)$$

After intersecting both planes for direct and reverse PTs, these conditions coincide. Note that for cubic-to-tetragonal transformation, there are two transformation strains $\varepsilon_{t1} = \varepsilon_{t2}$. Therefore, the coefficients for σ_1 and σ_2 in Eq. (21) are the same.

To make Eqs. (20) and (21) coincident, the second derivatives of all interpolation functions participating in (20) should be controlled by some prescribed values:

$$\frac{d^2\varphi_m(0)}{d\eta^2} = 2a_m \geq 0; \qquad \frac{d^2\varphi_m(1)}{d\eta^2} = 2w_m \leq 0. \quad (22)$$

2.4 Advanced interpolation function for transformation strain

In this section, we present an advanced interpolation function for transformation strain, which enables the PFA instability criteria Eq. (20) to reproduce the lattice instability conditions obtained by MD simulations in Eq. (21). It can be observed in Eq. (21) that the slopes of planes for direct and reverse PTs are different. According to results in [30,31,34], this

cannot be achieved by means of the traditional scalar interpolation function; the same applies to all components of the transformation strain. Thus, we need a matrix form of the interpolation function with a different function for each independent component of the transformation deformation gradient U_t. Besides, the minimum degree of polynomial that satisfies the three mentioned conditions for the interpolation function in Eqs. (15), (19), and (22), is a fifth degree polynomial.

The transformation deformation gradient can be obtained by interpolating the transformation strain as

$$
\begin{aligned}
U_t(\eta) &= I + \varepsilon_t \circ \varphi(a_\varepsilon, w_\varepsilon, \eta); \\
\varphi &:= [a_\varepsilon \eta^2 + (10\iota - 3a_\varepsilon + w_\varepsilon)\eta^3 \\
&\quad + (3a_\varepsilon - 2w_\varepsilon - 15\iota)\eta^4 + (6\iota - a_\varepsilon + w_\varepsilon)\eta^5],
\end{aligned}
\tag{23}
$$

where $\varepsilon_t = U_t(1) - I$ is the transformation strain after complete transformation from the parent phase P_0 to the product phase P_1; φ (and consequently, $a_\varepsilon, w_\varepsilon, \iota$) is a matrix (not a second-rank tensor), which has the same symmetry and non-zero components as ε_t in the coordinate system of the crystal lattice of P_1; all non-zero components of matrix ι are equal to 1. The Hadamard product is defined as $\varepsilon_t \circ \varphi := \{\varepsilon_{tij}\varphi^{ij}\}$ with no summation over i and j. Matrices a_ε and w_ε contain the constants of the interpolation function φ^{ij} to be found through the calibration of the lattice instability criteria with atomistic simulations. They are also equal to the second derivative of φ at $\eta = 0$ and $\eta = 1$, respectively. For transformations between cubic and tetragonal phases Si I $\leftrightarrow$ Si II, all matrices are defined in the cubic axes of Si I, all non-diagonal components are zero, and two diagonal components corresponding to the equal transformation strains are equal. Two independent constants in matrices a_ε and w_ε are given in Table 2.

Here, we simplify the PFA instability criteria and then show that with the presented advanced interpolation functions, they can produce the same instability conditions as in MD simulations. Because the MD simulations have shown that the shear stresses contribution in the lattice instability is negligible, we only consider the normal stress components. Substituting all terms in Eq. (20) and expressing the first Piola–Kirchhoff stress in terms of the Cauchy stress, we obtain the criteria for direct and reverse PTs as

$$
P_0 \rightarrow P_1 : \quad \left.\frac{\partial X}{\partial \eta}\right|_{\eta=0} \geq 0 \quad \Rightarrow
$$
$$
\left(\sigma - \frac{\psi^e}{J_e}I\right):\varepsilon_t \circ a_\varepsilon - \frac{1}{J_e}(A + 3\Delta\psi^\theta) \geq 0;
$$
$$
P_1 \rightarrow P_0 : \quad \left.\frac{\partial X}{\partial \eta}\right|_{\eta=1} \geq 0 \quad \Rightarrow
$$

$$
\left(\sigma - \frac{\psi^e}{J_e}I\right):U_t^{-1}(1)\cdot\varepsilon_t \circ w_\varepsilon - \frac{1}{J}(A - 3\Delta\psi^\theta) \geq 0.
\tag{24}
$$

In the next step, Eq. (24) can be expressed more explicitly. Because the MD instability criteria are linear in the stress components, and ψ^e is a nonlinear term in the stresses as well as being an order of magnitude smaller than the stresses, the term ψ^e can be neglected. The first term in Eq. (24) can be simplified further for cubic-to-tetragonal PT accounting for $\varepsilon_{t2} = \varepsilon_{t1}$ due to tetragonal symmetry. After these elaborations Eq. (24) simplifies as

$P_0 \rightarrow P_1 :$
$$
(\sigma_1 + \sigma_2)\varepsilon_{t1}a_{\varepsilon 1} + \sigma_3\varepsilon_{t3}a_{\varepsilon 3} \geq \frac{1}{J_e}(A + 3\Delta\psi^\theta);
$$
$P_1 \rightarrow P_0 :$
$$
(\sigma_1 + \sigma_2)\frac{\varepsilon_{t1}w_{\varepsilon 1}}{1 + \varepsilon_{t1}} + \frac{\sigma_3\varepsilon_{t3}w_{\varepsilon 3}}{1 + \varepsilon_{t3}} \geq \frac{1}{J}(A - 3\Delta\psi^\theta).
\tag{25}
$$

2.5 Specification of the elastic energy

Considering an orthotropic crystal, the simplest elastic energy can be given by [19]

$$
\begin{aligned}
\psi^e &= \frac{1}{2}E_e:C:E_e \\
&= \frac{1}{2}C^{ijkl}E_e^{ij}E_e^{kl} \\
&= \frac{1}{2}\sum_{n=1}^{3}\left[\lambda^n(E_e^{nn})^2 + 2\mu^n E_e^{nn}E_e^{kk} + 4\nu^n E_e^{nk}E_e^{kn}\right],
\end{aligned}
\tag{26}
$$

in which the 4th rank elastic moduli with three orthogonal symmetry planes have been considered as

$$
\begin{aligned}
C^{ijkl} = \sum_{n=1}^{3}[&\lambda^n \delta^{in}\delta^{jn}\delta^{kn}\delta^{ln} + \mu^n(\delta^{in}\delta^{jn}\delta^{kl} + \delta^{ij}\delta^{kn}\delta^{ln}) \\
&+ \nu^n(\delta^{in}\delta^{jk}\delta^{ln} + \delta^{jn}\delta^{ik}\delta^{ln} + \delta^{in}\delta^{jl}\delta^{kn} + \delta^{jn}\delta^{il}\delta^{kn})].
\end{aligned}
\tag{27}
$$

Here, the constants λ^n, μ^n and ν^n can be expressed in terms of nine independent elastic constants as

$$
\begin{aligned}
\lambda^1 &= C^{11} + C^{23} + 2C^{44} - (C^{12} + C^{13} + 2C^{55} + 2C^{66}), \\
\lambda^2 &= C^{22} + C^{13} + 2C^{55} - (C^{12} + C^{23} + 2C^{44} + 2C^{66}), \\
\lambda^3 &= C^{33} + C^{12} + 2C^{66} - (C^{13} + C^{23} + 2C^{44} + 2C^{55}), \\
2\mu^1 &= C^{12} + C^{13} - C^{23}, \qquad 2\nu^1 = C^{55} + C^{66} - C^{44}, \\
2\mu^2 &= C^{12} + C^{23} - C^{13}, \qquad 2\nu^1 = C^{44} + C^{66} - C^{55}, \\
2\mu^3 &= C^{13} + C^{23} - C^{12}, \qquad 2\nu^1 = C^{44} + C^{55} - C^{66}.
\end{aligned}
\tag{28}
$$

In particular, for a tetragonal crystal lattice, which has two equivalent symmetry planes, one has $C^{11} = C^{22}$, $C^{13} = C^{23}$, and $C^{44} = C^{55}$. Therefore, Eq. (28) simplifies to

$$
\begin{aligned}
&\lambda^1 = \lambda^2 = C^{11} - (C^{12} + 2C^{66}), \\
&\lambda^3 = C^{33} + C^{12} + 2C^{66} - 2(C^{13} + 2C^{44}), \\
&2\mu^1 = 2\mu^2 = C^{12}, \qquad 2\mu^3 = 2C^{13} - C^{12}, \\
&2\nu^1 = 2\nu^2 = C^{66}, \qquad 2\nu^3 = 2C^{44} - C^{66}.
\end{aligned}
\tag{29}
$$

Furthermore, for cubic crystals, all three orthogonal symmetry planes are equivalent; therefore, $C^{11} = C^{22} = C^{33}$, $C^{13} = C^{23} = C^{13}$, and $C^{44} = C^{55} = C^{66}$, and Eq. (28) reduces to

$$
\begin{aligned}
&\lambda^1 = \lambda^2 = \lambda^3 = C^{11} - C^{12} - 2C^{44}, \\
&2\mu^1 = 2\mu^2 = 2\mu^3 = C^{12}, \\
&2\nu^1 = 2\nu^2 = 2\nu^3 = C^{44}.
\end{aligned}
\tag{30}
$$

During the PT, the elastic constants λ^n, μ^n and ν^n for the three orthogonal directions are interpolated as

$$
\begin{aligned}
&\lambda^n = \lambda_0^n + (\lambda_1^n - \lambda_0^n)\varphi_e(\eta); \quad \mu^n = \mu_0^n + (\mu_1^n - \mu_0^n)\varphi_e(\eta); \\
&\nu^n = \nu_0^n + (\nu_1^n - \nu_0^n)\varphi_e(\eta),
\end{aligned}
\tag{31}
$$

using the elastic constants of P_0 and P_1, namely λ_0^n, μ_0^n, ν_0^n and λ_1^n, μ_1^n, and ν_1^n, respectively. The corresponding interpolation function is [27]:

$$
\varphi_e(\eta) = \eta^3(10 - 15\eta + 6\eta^2).
\tag{32}
$$

This interpolation function, having zero first and second derivatives at $\eta = 0$ and 1, has been used to eliminate the nonlinear term in stresses in the PFA instability criteria, which include change of elastic energy. The MD simulations of Si I $\leftrightarrow$ Si II PTs have resulted in linear-in-stresses instability conditions [36,37].

2.6 Boundary conditions for mechanics and phase field problems

Mechanics problem. We prescribe the displacements on S_{0u} and the traction on S_{0T}:

$$
\begin{aligned}
\boldsymbol{u} &= \bar{\boldsymbol{u}} \quad \text{on } S_{0u}, \quad \text{and} \tag{33} \\
\boldsymbol{P} \cdot \boldsymbol{n}_0 &= \bar{\boldsymbol{p}} \quad \text{on } S_{0T}, \tag{34}
\end{aligned}
$$

where $\bar{\boldsymbol{u}}$ and $\bar{\boldsymbol{p}}$ are the specified displacement vector and traction vector on the respective boundaries. The periodic boundary conditions for the displacements are also considered. If a pair of surfaces $S_{0u}^{P1} \subset S_0$ and $S_{0u}^{P2} \subset S_0$ have

periodic BCs for displacements (where $S_{0u}^{P1} \cap S_{0u}^{P2}$ is empty),

$$
\boldsymbol{u}|_{S_{0u}^{P1}} = \boldsymbol{u}|_{S_{0u}^{P2}} + D\boldsymbol{u},
\tag{35}
$$

where $D\boldsymbol{u}$ is specified. A mixed type of boundary conditions can also be used where, on a particular boundary, some component(s) of the displacements are specified, some component(s) of the traction vector are specified, and a part of the boundary has periodic BC on the displacements.
Phase field problem. For the phase field problem, we specify the order parameter η on the Dirichlet boundary, i.e.

$$
\eta = \bar{\eta} \quad \text{on } S_{0\eta}^D,
\tag{36}
$$

consider the homogeneous BC on the Neumann boundary

$$
\boldsymbol{\nabla}_0 \eta \cdot \boldsymbol{n}_0 = 0 \quad \text{on } S_{0\eta}^N,
\tag{37}
$$

and on a pair of periodic boundaries $S_{0\eta}^{P1} \subset S_0$ and $S_{0\eta}^{P1} \subset S_0$ (where $S_{0\eta}^{P1} \cap S_{0\eta}^{P2}$ is empty) having opposite outward unit normal vectors ($\boldsymbol{n}_0|_{S_{0\eta}^{P1}} = -\boldsymbol{n}_0|_{S_{0\eta}^{P2}}$), use the following conditions

$$
\eta|_{S_{0\eta}^{P1}} = \eta|_{S_{0\eta}^{P2}} \quad \text{and} \quad \boldsymbol{\nabla}_0 \eta \cdot \boldsymbol{n}_0|_{S_{0\eta}^{P1}} = -\boldsymbol{\nabla}_0 \eta \cdot \boldsymbol{n}_0|_{S_{0\eta}^{P2}}.
\tag{38}
$$

For a boundary-value problem, the boundary condition for the order parameter may be of Dirichlet type, Neumann type, periodic type, or a combination of any two types or all three types.

3 Weak formulations and finite element procedure

We have used a nonlinear finite element method for solving the coupled elasticity and phase field equation enlisted in Sect. 2. We have used a non-monolithic method to solve the systems of equations, i.e. while solving the mechanical equilibrium equations, we have assumed that the order parameter remains fixed, and while solving the Ginzburg–Landau equation, we have assumed that the state of deformation of the body is fixed.

3.1 Weak form of mechanical equilibrium equation and its linearization

The weak form of the equilibrium equation Eq. (13) is [48]

$$
R(\boldsymbol{u}, \delta\boldsymbol{u}) = -\int_{\Omega_0} (\boldsymbol{\nabla}_0 \cdot \boldsymbol{P}) \cdot \delta\boldsymbol{u} \, dV_0 = 0,
\tag{39}
$$

where $\delta\boldsymbol{u}$ is the virtual displacement (also called the test function), which satisfies $\delta\boldsymbol{u} = \boldsymbol{0}$ on the displacement boundary

S_{0u}. It is shown in the A that Eq. (39) can be rewritten in the following amenable form:

$$
\begin{aligned}
R(\boldsymbol{u}, \delta \boldsymbol{u}) &= \int_{\Omega_0} \boldsymbol{S} : \delta \boldsymbol{E} dV_0 - \int_{\Gamma_0} \bar{\boldsymbol{p}} \cdot \delta \boldsymbol{u} dS_0 \\
&= \int_{\Omega_0} \boldsymbol{\tau} : \delta \boldsymbol{\varepsilon} dV_0 - \int_{\Gamma_0} \bar{\boldsymbol{p}} \cdot \delta \boldsymbol{u} dS_0 = 0,
\end{aligned}
\tag{40}
$$

where $\boldsymbol{\tau} = J\boldsymbol{\sigma}$ is the Kirchhoff stress and

$$
\delta \boldsymbol{\varepsilon} = \frac{1}{2}(\nabla \delta \boldsymbol{u}^T + \nabla \delta \boldsymbol{u}).
\tag{41}
$$

To solve for the displacements using the Newton's iterative method we linearize the weak form Eq. (40) and obtain (see A for details)

$$
\begin{aligned}
DR \cdot \Delta \boldsymbol{u} &= \int_{\Omega_0} \delta \boldsymbol{\varepsilon} : J\mathsf{C} : \Delta \boldsymbol{\varepsilon} dV_0 \\
&+ \int_{\Omega_0} \nabla \delta \boldsymbol{u} : \boldsymbol{\tau} \cdot \nabla \Delta \boldsymbol{u}^T dV_0,
\end{aligned}
\tag{42}
$$

where $\Delta \boldsymbol{u}$ is an increment of the displacement vector and C is the fourth-order elasticity tensor defined in Ω which is related to $\mathcal{C}$ and $\boldsymbol{C}$, the fourth-order elastic modulus tensors defined in Ω_0 and Ω_t respectively (see Eqs. 27–32) through

$$
\begin{aligned}
\mathsf{C}^{\hat{i}\hat{j}\hat{k}\hat{l}} &= \frac{1}{J} F^{\hat{i}I} F^{\hat{j}J} F^{\hat{k}K} F^{\hat{l}L} \mathcal{C}^{IJKL} \\
&= \frac{1}{J_e} F_e^{\hat{i}i} F_e^{\hat{j}j} F_e^{\hat{k}k} F_e^{\hat{l}l} C^{ijkl}.
\end{aligned}
\tag{43}
$$

Note that the indices in upper case, i.e. I, J, etc. are for Ω_0; the indices in lower case i, j, etc. are for Ω_t; and the indices with 'hat', i.e. $\hat{i}$, $\hat{j}$, etc. are used for the deformed configuration Ω. The modulus $\boldsymbol{C}$ is defined as

$$
\boldsymbol{C} := \frac{\partial \hat{\boldsymbol{S}}}{\partial \boldsymbol{E}_e} = \frac{\partial^2 \psi^e}{\partial \boldsymbol{E}_e \partial \boldsymbol{E}_e}.
\tag{44}
$$

In Eq. (42), $\Delta \boldsymbol{\varepsilon}$ is defined as

$$
\Delta \boldsymbol{\varepsilon} := 0.5(\nabla \Delta \boldsymbol{u} + \nabla \Delta \boldsymbol{u}^T).
\tag{45}
$$

3.2 Weak form of Ginzburg–Landau equation and its linearization

We will now derive the weak form of the Ginzburg–Landau equation (12) and linearize it. To this end we discretize the time derivative using $\dot{\eta} = (\eta_n - \eta_{n-1})/k$ over the time interval $t_0 \le t \le t_f$, where k is the time step size, t_0 is the initial time, and t_f is the final time. We thus discretize the Ginzburg–Landau equation (12) and express it as

$$
\frac{\eta_n - \eta_{n-1}}{Lk} + f_n - \beta \nabla_0^2 \tilde{\eta}_n = 0,
\tag{46}
$$

where $\tilde{\eta}_n = \vartheta \eta_n + (1 - \vartheta)\eta_{n-1}$, the subscript n denotes the time step number, and the function f_n is given by

$$
\begin{aligned}
f_n &= f(\tilde{\eta}_n, \boldsymbol{u}_{n-1}) \\
&= - \left(\boldsymbol{P}_n^T \cdot \boldsymbol{F}_{n-1} - J_{tn}(\tilde{\eta}_n)\psi^e(\boldsymbol{E}_{en}, \tilde{\eta}_n)\boldsymbol{I} \right) : \boldsymbol{U}_{tn}^{-1}(\tilde{\eta}_n) \\
&\quad \cdot \frac{\partial \boldsymbol{U}_t(\tilde{\eta}_n)}{\partial \eta} + J_{tn}(\tilde{\eta}_n)\frac{\partial \psi^e(\tilde{\eta}_n)}{\partial \eta}\Big|_{\boldsymbol{E}_e} + \frac{\partial \psi^\theta(\tilde{\eta}_n)}{\partial \eta}.
\end{aligned}
\tag{47}
$$

Note that the Ginzburg–Landau equation is discretized in time using the ϑ-method, which allows for a continuum of the scheme. For instance, choosing $\vartheta = 0$ or $\vartheta = 1$, we receive an explicit or implicit Euler method, respectively, where both methods are first-order schemes. However, $\vartheta = 0.5$ leads to a second-order scheme, called the Crank–Nicolson method. It should be noticed that the local driving force X at the right-hand side causes nonlinearity. Besides, the zero Neumann boundary condition is enforced, there is no Dirichlet boundary condition, and in the case of Periodic BC, it is enforced as explained in Eq. (38) . We now write the weak form of the time-discretized equation (46) as

$$
\begin{aligned}
R_\eta(\eta_n, \delta\eta_n) &= \int_{\Omega_0} \frac{1}{L}\eta_n \delta\eta_n dV_0 - k\int_{\Omega_0} \beta\delta\eta_n \nabla_0^2 \tilde{\eta}_n \, dV_0 \\
&+ k\int_{\Omega_0} f(\tilde{\eta}_n, \boldsymbol{u}_{n-1})\delta\eta_n dV_0 \\
&- \int_{\Omega_0} \frac{1}{L}\eta_{n-1}\delta\eta_n dV_0 = 0,
\end{aligned}
\tag{48}
$$

Using the identity $\nabla_0 \cdot (\nabla_0 \tilde{\eta}_n \cdot \delta\eta_n) = \nabla_0^2 \tilde{\eta}_n \cdot \delta\eta_n + \nabla_0 \tilde{\eta}_n \cdot \nabla_0 \delta\eta_n$ in the second integral of Eq. (48) and applying the Gauss divergence theorem, we rewrite the general weak form of Eq. (48) as

$$
\begin{aligned}
R_\eta(\eta_n, \delta\eta_n) &= \int_{\Omega_0} \frac{1}{L}\eta_n \delta\eta_n dV_0 \\
&+ k\int_{\Omega_0} \beta\nabla_0\delta\eta_n \cdot \nabla_0 \tilde{\eta}_n \, dV_0 \\
&+ k\int_{\Omega_0} f(\tilde{\eta}_n, \boldsymbol{u}_{n-1}) \, \delta\eta_n dV_0 \\
&- \int_{\Omega_0} \frac{1}{L}\eta_{n-1}\delta\eta_n dV_0 \\
&- k\int_{S_0 \setminus S_{0\eta}^D} \beta\delta\eta_n \nabla_0 \tilde{\eta}_n \cdot \boldsymbol{n}_0 \, dS_0 = 0,
\end{aligned}
\tag{49}
$$

where, in the last integral, we have used the fact that $\delta\eta = 0$ at the Dirichlet boundary and hence the integration is to be performed over the homogeneous Neumann boundary and/or the periodic boundaries if there are any (see Sect. 2.6). If there are periodic boundaries, applying conditions in Eq. (38) the last integration in Eq. (49) is further simplified to only be taken over the Neumann boundaries $S_{0\eta}^N$.

In both cases from Eqs. (37) and (38)$_2$, we conclude that the last integral in Eq. (49) identically vanishes.

We will use the Newton's iteration method for computing the order parameter in a manner similar to the mechanics problem. To do so, we will linearize the weak form given by Eq. (49) and determine the tangent. The weak form is expanded in the Taylor' series about η_k^n:

$$
\mathcal{R}_\eta(\eta_n + \Delta_\eta\eta_n, \delta\eta_n) = \mathcal{R}_\eta(\eta_n, \delta\eta_n) \\
+ \Delta_\eta\mathcal{R}_\eta + o(\Delta_\eta\eta_n) = 0, \tag{50}
$$

where Δ_η denotes the increment of a function or functional with respect to η and $o(\Delta_\eta\eta_n)$ is such that $\lim_{\Delta_\eta\eta_n \to 0} o(\Delta_\eta\eta_n)/\Delta_\eta\eta_n = 0$. Using Eq. (48) we derive (note that the last integral therein is zero)

$$
\Delta_\eta R_\eta = \left.\frac{\partial R_\eta}{\partial \eta_n}\right|_F \Delta_\eta\eta_n \\
= \int_{\Omega_0} \frac{1}{L} \Delta_\eta\eta_n \, \delta\eta_n dV_0 \\
+ k\vartheta \int_{\Omega_0} \beta \nabla_0(\Delta_\eta\eta_n) \cdot \nabla_0\delta\eta_k^n dV_0 \\
+ k \int_{\Omega_0} \left.\frac{\partial f_n}{\partial \eta_n}\right|_F \Delta_\eta\eta_n\delta\eta_n dV_0, \tag{51}
$$

where, using the chain rule for differentiation we obtain

$$
\left.\frac{\partial f_n}{\partial \eta_n}\right|_F = \vartheta \left.\frac{\partial f_n}{\partial \tilde\eta_n}\right|_F \\
= -\vartheta \left(P_n^T \cdot F_{n-1} - J_{tn}\psi^e(E_{en}, \tilde\eta_n)I\right) : \left(U_{tn}^{-1} \cdot \frac{\partial^2 U_{tn}}{\partial \tilde\eta_n^2} - W_n^2\right) \\
- \vartheta \left.\frac{\partial P_n^T}{\partial \tilde\eta_n}\right|_F \cdot F_{n-1} : W_n \\
+ \vartheta J_{tn}(\tilde\eta_n)\psi^e(E_{en}, \tilde\eta_n)(tr W_n)^2 \\
+ \vartheta J_{tn} \left(\left.\frac{\partial \psi^e(E_{en}, \tilde\eta_n)}{\partial \tilde\eta_n}\right|_F + \left.\frac{\partial \psi^e(E_{en}, \tilde\eta_n)}{\partial \tilde\eta_n}\right|_{E_e}\right) tr W_n \\
+ \vartheta J_{tn} \frac{\partial}{\partial \tilde\eta_n} \left(\left.\frac{\partial \psi^e(E_{en}, \tilde\eta_n)}{\partial \tilde\eta_n}\right|_{E_e}\right)_F + \vartheta\rho_0\Delta\psi^\theta(6 - 12\tilde\eta_n) \\
+ \vartheta\rho_0 A(2 - 12\tilde\eta_n + 12\tilde\eta_n^2), \tag{52}
$$

where

$$
W_n(\tilde\eta_n) = U_{tn}^{-1}(\tilde\eta_n) \cdot \frac{\partial U_{tn}(\tilde\eta_n)}{\partial \tilde\eta_n}, \tag{53}
$$

$$
\left.\frac{\partial P_n^T}{\partial \tilde\eta_n}\right|_F = \left[J_{tn}(tr W_n)U_{tn}^{-1} \cdot \hat S_n \cdot U_{tn}^{-1} - 2 sym(S_n \cdot W_n)\right. \\
\left. + J_{tn}U_{tn}^{-1} \cdot \left.\frac{\partial \hat S_n}{\partial \tilde\eta_n}\right|_F \cdot U_{tn}^{-1}\right] \cdot F_{n-1}^T, \tag{54}
$$

$$
\left.\frac{\partial \hat S_n}{\partial \tilde\eta_n}\right|_F = \frac{\partial C_n(\tilde\eta_n)}{\partial \tilde\eta_n} : E_{en} + C_n(\tilde\eta_n) : \left.\frac{\partial E_{en}}{\partial \tilde\eta_n}\right|_F, \tag{55}
$$

$$
\left.\frac{\partial E_{en}}{\partial \tilde\eta_n}\right|_F = -sym\left(F_{en}^T \cdot F_{en} \cdot \frac{\partial U_{tn}(\tilde\eta_n)}{\partial \tilde\eta_n} \cdot U_{tn}^{-1}(\tilde\eta_n)\right), \tag{56}
$$

$$
\left.\frac{\partial \psi_{en}}{\partial \tilde\eta_n}\right|_{E_e} = \frac{1}{2}E_{en} : \left.\frac{\partial C_n}{\partial \tilde\eta_n}\right|_{E_e} : E_{en}, \tag{57}
$$

$$
\left.\frac{\partial \psi_{en}}{\partial \tilde\eta_n}\right|_F = \frac{1}{2}E_{en} : \left.\frac{\partial C_n}{\partial \tilde\eta_n}\right|_F : E_{en} \\
+ E_{en} : C_n(\tilde\eta_n) : \left.\frac{\partial E_{en}}{\partial \tilde\eta_n}\right|_F, \quad \text{and} \tag{58}
$$

$$
\frac{\partial}{\partial \tilde\eta_n}\left(\left.\frac{\partial \psi_{en}}{\partial \tilde\eta_n}\right|_{E_e}\right)_F = \frac{1}{2}E_{en} : \frac{\partial^2 C_n(\tilde\eta_n)}{\partial \tilde\eta_n^2} : E_{en} \\
+ E_{en} : \frac{\partial C_n(\tilde\eta_n)}{\partial \tilde\eta_n} : \left.\frac{\partial E_{en}}{\partial \tilde\eta_n}\right|_F. \tag{59}
$$

Note that we have used $P_n = J_{tn}F_{n-1} \cdot U_{tn}^{-1} \cdot \hat S_n \cdot U_{tn}^{-1}$ to obtain the expression in Eq. (54), and to calculate the derivative of E_{en} with respect to $\tilde\eta_n$, we used Eq. (3)$_4$.

3.3 Finite element implementation

We will now derive the finite element equations. The reference body Ω_0 is discretized into n_{el} number of elements $\Omega_0 \approx \cup_{el=1}^{n_{el}}\Omega_0^{el}$. Assuming isoparametric elements, we accept the following interpolations for the position vectors, displacements, order parameter, and the variations and increments of the variables in each element Ω_0^{el} (see e.g. [48]):

$$
r_0^{el} = \sum_{a=1}^{n_g} N_a(\xi)\tilde r_{0a}, \quad r^{el} = \sum_{a=1}^{n_g} N_a(\xi)\tilde r_a,
$$

$$
u^{el} = \sum_{a=1}^{n_g} N_a(u)\tilde u_a,
$$

$$
\delta u^{el} = \sum_{a=1}^{n_g} N_a(\xi)\delta\tilde u_a, \quad \Delta u^{el} = \sum_{a=1}^{n_g} N_a(\xi)\Delta\tilde u_a,
$$

$$
\eta^{el} = \sum_{a=1}^{n_g} N_a(\xi)\tilde\eta_a,
$$

$$
\delta\eta^{el} = \sum_{a=1}^{n_g} N_a(\xi)\delta\tilde\eta_a, \quad \Delta_\eta\eta^{el} = \sum_{a=1}^{n_g} N_a(\xi)\Delta_\eta\tilde\eta_a. \tag{60}
$$

In Eq. (60), N_a ($a = 1, 2, \ldots, n_g$) denote the shape functions for the element Ω_0^{el}; n_g is the number of nodal points in each element; the quantity with tilde corresponding to each variable denotes its nodal value; e.g. $\tilde r_{0a}$ denotes the displacement vector at ath node; the superscript el designates the index for the elements; and ξ designates the coordinate of

an isoparametric element in its reference configuration [48]. The gradients of the displacement vector, order parameter, variation, and increment of the variables are obtained as [48]

$$\nabla \boldsymbol{u}^{el} = \sum_{a=1}^{n_g} \tilde{\boldsymbol{u}}_a \otimes \boldsymbol{j}^{el-T} \cdot \nabla_\xi N_a,$$

$$\nabla \delta \boldsymbol{u}^{el} = \sum_{a=1}^{n_g} \delta \tilde{\boldsymbol{u}}_a \otimes \boldsymbol{j}^{el-T} \cdot \nabla_\xi N_a,$$

$$\nabla \Delta \boldsymbol{u}^{el} = \sum_{a=1}^{n_g} \Delta \tilde{\boldsymbol{u}}_a \otimes \boldsymbol{j}^{el-T} \cdot \nabla_\xi N_a,$$

$$\nabla \eta^{el} = \sum_{a=1}^{n_g} \tilde{\eta}_a \, \boldsymbol{j}^{el-T} \cdot \nabla_\xi N_a,$$

$$\nabla \delta \eta^{el} = \sum_{a=1}^{n_g} \delta \tilde{\eta}_a \, \boldsymbol{j}^{el-T} \cdot \nabla_\xi N_a,$$

$$\nabla \Delta_\eta \eta^{el} = \sum_{a=1}^{n_g} \Delta_\eta \tilde{\eta}_a \, \boldsymbol{j}^{el-T} \cdot \nabla_\xi N_a, \tag{61}$$

where $\boldsymbol{j}^{el} = \frac{\partial \boldsymbol{r}^{el}}{\partial \boldsymbol{\xi}} = \sum_{a=1}^{n_g} \tilde{\boldsymbol{r}}_a \otimes \nabla_\xi N_a$, ∇_ξ designates the gradient with respect to the coordinates of the isoparametric element denoted by $\boldsymbol{\xi} = \{\xi_1, \xi_2, \xi_3\}^T$, and therefore $\nabla_\xi N_a = [\partial N_a/\partial \xi_1, \, \partial N_a/\partial \xi_2, \, \partial N_a/\partial \xi_3]^T$.

3.3.1 Discretization of equilibrium equation and phase field equation

We will now use Eqs. (60) and (61) in the weak forms and their linearizations to derive the finite element equations. For the mechanics problem we use Eqs. (40) in (78), discretize it using Eqs. (60) and (61), and perform the assembly operation over all finite elements to obtain the system of algebraic equations given by Eq. (62), where we have neglected the higher order terms in $\Delta \boldsymbol{u}$ in Eq. (78) and used the arbitrariness of the increment of the nodal displacements. Note that $\boldsymbol{K}$ and $\boldsymbol{r}_u$, which are given by Eqs. $(63)_1$ and $(63)_2$ are the $n_u \times n_u$ global tangent matrix and $n_u \times 1$ global residual matrix, respectively, where n_u is the total number of displacement degrees of freedom. The expressions for the spatial gradient of the shape function and the standard FE $\boldsymbol{B}$ matrix are given by Eqs. $(64)_1$ and $(64)_2$, respectively, where the subscripts followed by a comma denote the spatial derivatives with respect to the corresponding coordinate in Ω. The geometric stiffness part of the total tangent matrix is given by Eq. $(63)_4$, which is neglected in the infinitesimal strain formulations. In Eq. (62), the central dot implies the standard multiplication between the matrix $\boldsymbol{K}$ and the column matrix $\Delta \boldsymbol{u}^p$. The nodal displacements after the pth iteration are computed using Eq. (65); see the algorithm in Sect. 3.4 for the procedure.

In a similar way we discretize the phase field problem. Using Eqs. (49) in (50), then using Eqs. (60) and (61) therein and performing the standard assembly operation, and utilizing the arbitrariness of the nodal increment of the order parameter, the system of equations given by Eq. (66) is obtained. Here $\boldsymbol{Q}$ is the $n_\eta \times n_\eta$ global symmetric matrix given by Eq. (72), $\boldsymbol{\eta}_n^q$ is the column matrix (global matrix of size $n_\eta \times 1$) of the nodal order parameter after the qth iteration, the column matrix (global) $\Delta \boldsymbol{\eta}_n^q$ of size $n_\eta \times 1$ contains the increment of the order parameter, and n_η is the total number of DOF for η in the domain. The order parameter is then updated using Eq. (73). The explicit expressions for the global symmetric matrices $\boldsymbol{M}$, $\boldsymbol{L}$, and $\boldsymbol{G}$ of size $n_\eta \times n_\eta$ and the global column matrices $\boldsymbol{f}$ and $\boldsymbol{r}$ of size $n_\eta \times 1$ are given in Box-I. We will solve Eq. (66) iteratively and update the order parameters at every time step using Eq. (73) while keeping the state of deformation of the body fixed. The procedure is outlined in Sect. 3.4.

Box-I. Finite element equations for mechanics and phase field problem

- A system of algebraic equations for computing the increment of the nodal displacements at the pth Newton iteration

$$\boldsymbol{K} \cdot \Delta \boldsymbol{u}^p = -\boldsymbol{r}_u, \quad \text{where} \tag{62}$$

$$\boldsymbol{K}(\boldsymbol{u}^{p-1}) = \bigcup_{el=1}^{n_{el}} \sum_{a=1}^{n} \sum_{b=1}^{n} \int_{\Omega^{el}} (G_{ab}\boldsymbol{I} + \boldsymbol{B}_a^T \mathsf{C}^{el} \boldsymbol{B}_b) \, dV_0,$$

$$\boldsymbol{r}_u(\boldsymbol{u}^{p-1}) = \bigcup_{el=1}^{n_{el}} \sum_{a=1}^{n} \int_{\Omega^{el}} \boldsymbol{B}_a^T \boldsymbol{\tau}^{el} \, dV_0,$$

$$G_{ab}\boldsymbol{I} = (\nabla N_a \cdot \boldsymbol{\tau}^{el} \cdot \nabla N_b) \, \boldsymbol{I},$$

$$\mathsf{C}^{\hat{i}\hat{j}\hat{k}\hat{l}} = \frac{1}{J} F^{\hat{i}I} F^{\hat{j}J} F^{\hat{k}K} F^{\hat{l}L} C^{IJKL}$$

$$= \frac{1}{J_e} F_e^{\hat{i}i} F_e^{\hat{j}j} F_e^{\hat{k}k} F_e^{\hat{l}l} C^{ijkl}. \tag{63}$$

Gradient of shape function and $\boldsymbol{B}$ matrix

$$\nabla N_a = \begin{bmatrix} N_{a,1} \\ N_{a,2} \\ N_{a,3} \end{bmatrix}, \qquad \boldsymbol{B}_a = \begin{bmatrix} N_{a,1} & 0 & 0 \\ 0 & N_{a,2} & 0 \\ 0 & 0 & N_{a,3} \\ N_{a,2} & N_{a,1} & 0 \\ 0 & N_{a,3} & N_{a,2} \\ N_{a,3} & 0 & N_{a,1} \end{bmatrix}. \tag{64}$$

The nodal displacements are updated after the pth iteration using

$$\boldsymbol{u}^p = \boldsymbol{u}^{p-1} + \Delta \boldsymbol{u}^p. \tag{65}$$

- A system of algebraic equations for increment of the nodal order parameters

$$\boldsymbol{Q} \cdot \Delta_\eta \boldsymbol{\eta}_n^q = -\boldsymbol{r}_\eta, \quad \text{where} \tag{66}$$

$$\boldsymbol{Q}(\eta_n^{p-1}) = \boldsymbol{M} + k\,\vartheta\,\boldsymbol{L} + k\,\boldsymbol{G}, \tag{67}$$

$$\boldsymbol{M} = \bigcup_{el=1}^{n_{el}} \sum_{a=1}^{n_g} \sum_{b=1}^{n_g} \int_{\Omega_0^{el}} \frac{1}{L} N_a N_b dV_0, \tag{68}$$

$$\boldsymbol{L} = \bigcup_{el=1}^{n_{el}} \sum_{a=1}^{n_g} \sum_{b=1}^{n_g} \int_{\Omega_0^{el}} \beta \left(\boldsymbol{\nabla}_0 N_a \cdot \boldsymbol{\nabla}_0 N_b\right) dV_0, \tag{69}$$

$$\boldsymbol{G}(\eta_n^{p-1}) = \bigcup_{el=1}^{n_{el}} \sum_{a=1}^{n_g} \sum_{b=1}^{n_g} \int_{\Omega_0^{el}} \left.\frac{\partial f_n(\eta_n^{p-1})}{\partial \eta_n}\right|_{\boldsymbol{F}} N_a N_b dV_0, \tag{70}$$

$$\boldsymbol{r}_\eta(\eta_n^{p-1}) = \{\boldsymbol{M} + k\,\vartheta\,\boldsymbol{L}\} \cdot \boldsymbol{\eta}_n^{p-1}$$
$$\qquad - \{\boldsymbol{M} - (1-\vartheta)k\,\boldsymbol{L}\} \cdot \boldsymbol{\eta}_{n-1} + k\,\boldsymbol{f}, \tag{71}$$

$$\boldsymbol{f}(\eta_n^{p-1}) = \bigcup_{el=1}^{n_{el}} \sum_{a=1}^{n_g} \int_{\Omega_0^{el}} f_n(\eta_n^{p-1}, \boldsymbol{u}_{n-1}) N_a dV_0. \tag{72}$$

The order parameters are updated using

$$\boldsymbol{\eta}_n^q = \boldsymbol{\eta}_n^{q-1} + \Delta_\eta \boldsymbol{\eta}_n^q. \tag{73}$$

3.4 Algorithm for computation

Here we outline the overall computational algorithm for solving the coupled Ginzburg–Landau equation and the mechanics equations. The geometry of the domain and all the initial data and model parameters are assumed to be known. The following symbols are used in the description of the procedure: t^n - time instance after the $(n-1)$th iteration (note that $t^0 = 0$); t^f - final time; ϵ_u — tolerance for checking the convergence of the mechanical equilibrium equation; ϵ_η - tolerance for checking the convergence of the phase field equation; and N^{max} - maximum number of iterations allowed for the Ginzburg–Landau equation.

WHILE $(t^n \leq t^f)$
{

1. # Newton's iteration for displacements (p is the index for iteration)

Take $p = 0$ and $\boldsymbol{u}^{n,0} = \boldsymbol{u}^{n-1}$
   DO{

- Set $p \to p + 1$

- Update $\boldsymbol{F}_n^{p-1} = \boldsymbol{I} + \boldsymbol{\nabla}_0 \boldsymbol{u}_n^{p-1}$ using Eq. $(1)_1$ and compute $\boldsymbol{U}_{tn}(\eta_{n-1})$ using Eq. (23_1) or Eq. $(??_1)$ based on the model at hand
- Update $\boldsymbol{F}_e$ using Eq. $(1)_2$ and $\boldsymbol{\sigma}$ using Eqs. $(10)_{2,3}$ and (26)
- Compute $\boldsymbol{K}(\boldsymbol{u}_n^{p-1})$ and $\boldsymbol{r}_u(\boldsymbol{u}_n^{p-1})$ using Eqs. $(63)_1$ and $(63)_2$
- Solve the linear system of Eq (62), i.e. $\boldsymbol{K}(\boldsymbol{u}_n^{p-1}) \cdot \Delta \boldsymbol{u}_n^p = -\boldsymbol{r}_u(\boldsymbol{u}_n^{p-1})$ to obtain $\Delta \boldsymbol{u}_n^p$
- Update the displacements using Eq. (65), i.e. $\boldsymbol{u}_n^p = \boldsymbol{u}_n^{p-1} + \Delta \boldsymbol{u}_n^p$
- Calculate the Euclidean norms of the residuals $|\boldsymbol{r}_u(\boldsymbol{u}_n^p)|$ and $|\boldsymbol{r}_u(\boldsymbol{u}_n^1)|$

}WHILE $(|\boldsymbol{r}_u(\boldsymbol{u}_n^p)| \leq \epsilon_u \times |\boldsymbol{r}_u(\boldsymbol{u}_n^1)|)$
   Set $n \to n + 1$

2. # Newton's iteration for the phase field equation (q is the index for iteration)
   Take $q = 0$, and $\boldsymbol{\eta}_n^0 = \boldsymbol{\eta}_{n-1}$
   Compute $\boldsymbol{F}(\boldsymbol{u}_{n-1})$ using Eq. $(1)_1$, i.e. $\boldsymbol{F}(\boldsymbol{u}_{n-1}) = \boldsymbol{I} + \boldsymbol{\nabla}_0 \boldsymbol{u}_{n-1}$

DO {

(a) Set $q \to q + 1$
(b) Compute $\boldsymbol{U}_t(\eta_n^{q-1})$ using Eq. (23_1) or Eq. $(??_1)$, $\boldsymbol{F}_e$ using Eq. $(1)_2$, and $\boldsymbol{\sigma}$ using Eqs. $(10)_{2,3}$ and (26)
(c) Compute the matrices $\boldsymbol{Q}(\eta_n^{q-1})$, $\boldsymbol{M}(\eta_n^{q-1})$, $\boldsymbol{L}(\eta_n^{q-1})$, $\boldsymbol{G}(\eta_n^{q-1})$, $\boldsymbol{f}(\eta_n^{q-1})$, and $\boldsymbol{r}_\eta(\eta_n^{q-1})$ listed in Box-I
(d) Solve Eq. (66), i.e. $\boldsymbol{Q} \cdot \Delta_\eta \boldsymbol{\eta}_n^q = -\boldsymbol{r}_\eta$ to obtain $\Delta_\eta \boldsymbol{\eta}_n^q$
(e) Update $\boldsymbol{\eta}_n^q$ using Eq. (73), i.e. $\boldsymbol{\eta}_n^q = \boldsymbol{\eta}_n^{q-1} + \Delta_\eta \boldsymbol{\eta}_n^q$
(f) Compute the Euclidean norms of the residual $|\boldsymbol{r}_\eta(\eta_n^q)|$

}WHILE $(|\boldsymbol{r}_\eta(\eta_n^q)| \leq \epsilon_\eta \times |\boldsymbol{r}_\eta(\eta_n^1)|)$
}

4 Material parameters for Si I $\leftrightarrow$ Si II phase transformations

The material parameters taken from [11,34] are used and listed in Table 1. The thermal driving force for PT $\Delta\psi^\theta$, the transformation strain $\boldsymbol{\varepsilon}_t$, and the double-well barrier constant A, along with the constants in the interpolation function for transformation strain $a_{\varepsilon 1}$, $a_{\varepsilon 3}$, $w_{\varepsilon 1}$, and $w_{\varepsilon 3}$, are obtained from PFA calibration [2,27] using results from the MD simulations [36,37] and are listed in Table 2. In particular, the Si I $\leftrightarrow$ Si II transformation strain measures are $\boldsymbol{\varepsilon}_t = (0.1753; 0.1753; -0.447)$. Therefore, $J_t(1) = (1 + \varepsilon_{t1})^2(1 + \varepsilon_{t3}) = 0.764$. For calibration, the Jacobian

Table 1 Material parameters including kinetic coefficient L $(Pa\,s)^{-1}$, gradient energy constant β (N) and elastic constants (GPa)

L	β	C_0^{11}	C_0^{44}	C_0^{12}	C_1^{11}	C_1^{33}	C_1^{44}	C_1^{66}	C_1^{12}	C_1^{13}
2600	2.59×10^{-10}	167.5	80.1	65.0	174.76	136.68	60.24	42.22	102.0	68.0

Table 2 Parameters obtained after calibration of the model with MD simulations

Stress state	$\Delta\psi^\theta$	A	$a_{\varepsilon 1}$	$a_{\varepsilon 3}$	$w_{\varepsilon 1}$	$w_{\varepsilon 3}$
If $-\sigma_3 \geq 6.23$	6.35	0.75	3.31	3.60	-2.48	-2.39
Otherwise	6.35	-9.48	1.10	2.26	-3.88	-3.73

$\Delta\psi^\theta$ and and A are presented in GPa

determinants, J_e and J in Eqs. (25) are considered to be 0.93 and 0.64 respectively, based on their magnitude in our PFA simulations of Si I $\leftrightarrow$ Si II PT.

5 Numerical solutions

The FEM algorithm and numerical procedure has been developed in the deal.II program [3], a C++ library aimed at the computational solution of partial differential equations. The three-dimensional, fully geometrically nonlinear response of an anisotropic crystal has been modeled. While the simulations are performed in the reference configuration, the results are presented in the deformed configuration. Finite element discretization was performed only at the beginning without remeshing during deformation.

5.1 Effect of different prescribed stress measures on lattice instability and initiation of the phase transformation

It is known that, for large strains, the elastic instability conditions depend on which stress measure is prescribed [12, 39,46]. However, it has been strictly mathematically proven that our PFA instability criteria are independent of the type of prescribed stress measure [22,27]. Here, we further analyze further this difference between our theory and previous theories. For this purpose, three different loading conditions including strain-controlled, Cauchy stress-controlled, and first Piola–Kirchhoff stress-controlled loadings are compared. We consider a *single 3D cubic finite element* with zero stresses on its four lateral faces and a homogeneous solution for stresses and strains. First, by controlling displacement on the top and bottom faces, a compressive strain-controlled loading in the vertical direction is applied. As a result, the three stress–strain curves for the Cauchy, first Piola–Kirchhoff, and second Piola–Kirchhoff stresses are obtained as shown in Fig. 1. Within the framework of our PFA, the
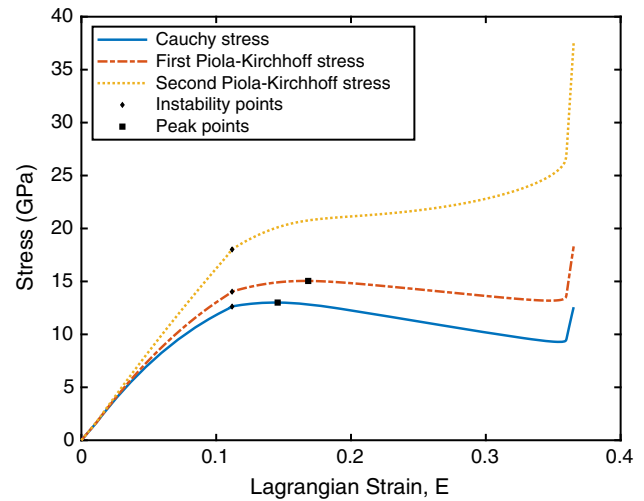

Fig. 1 Stress–strain curves for uniaxial compressive strain-controlled loading for three different stress tensors, Cauchy, first Piola–Kirchhoff and second Piola–Kirchhoff stresses. Markers show corresponding instability points and stress peak points

instability point for direct PT corresponds to the deviation of the order parameter from zero, i.e. to the initiation of a PT. While such a process does not occur spontaneously at fixed strain, we can achieve a "controlled instability." That is, we define instability as a strain state at which the driving force for the change of order parameter X, becomes positive and fluctuational deviation of the order parameter from zero does not return. This can be considered at fixed strain or any stress measure. It can be observed that such an instability occurs at a specific strain whose corresponding stresses are marked in Fig. 1 for all stress measures. Therefore, through this process, the instability stresses for different stress measures are obtained. Besides, it can be observed that the stress peaks do not coincide with instability points at larger strains.

Next, we consider two different stress-controlled loadings prescribing Cauchy stress and first Piola–Kirchhoff stress on the top and bottom faces of the element instead of displacement. The stress-order parameter curves for both stress-controlled measures as well as the strain-order parameter curve for the previous strain-controlled loading are shown in Fig. 2. It is apparent that, for both stress measures, once the stress exceeds the corresponding instability stress obtained in strain-controlled case, the driving force becomes positive and order parameter ceases to be zero and rises. However, this does not mean that, by exceeding the instability stress, the order parameter continues to rise until the PT is completed. If
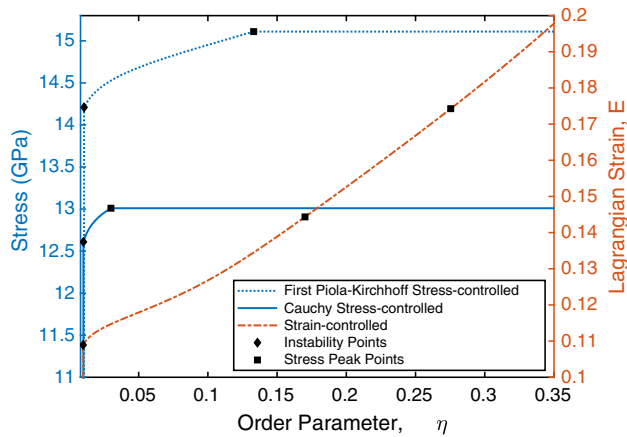
Fig. 2 Stress-order parameter curves for uniaxial compressive stress-controlled loadings with prescribed Cauchy or first Piola–Kirchhoff stresses. Strain-order parameter curve is also included for strain-controlled loading

we apply a stress that is higher than the instability stress but lower than the peak stress, the order parameter equilibrates at the corresponding value of the prescribed stress and remains constant. To have a continuing PT, the stress must slightly exceed the peak point so that afterward, the PT does not stop until completion. In addition, it can be observed from the strain-order parameter curve obtained in a strain-controlled loading that the strain must increase after instability to complete the PT, independent of the location of the stress peaks for both stress measures.

Thus, the instability point, at which PT starts and the order-parameter ceases to be zero, occurs at a specific strain and independent of the prescribed stress measure. However, to complete the PT, the stress should exceed the stress peak point depending on which stress measure is prescribed. The difference between our approach to lattice instability and the elastic instability approach in [12,39,46] is related to different definitions of instability. Our definition means instability of the phase equilibrium and initiation of a phase transformation. The elastic instability is related to the impossibility of mechanical equilibrium of the state under study and transition to other equilibrium state(s). As is illustrated in Fig. 1, mechanical instability, corresponding to the peak stress, clearly depends on the type of the prescribed stress measure.

During the solution of *boundary-value problems with heterogeneous fields*, we cannot prescribe stress for each material point within the bulk but only at the boundary. To further clarify the instability concept, let us consider a PT simulation shown in Fig. 3, in which a 3D sample of the size $20 \times 60 \times 5 \, \text{nm}^3$ is considered with values of the order parameter, randomly distributed in the range 0–0.1, as the initial condition to mimic the athermal heterogeneous perturbations. The right and bottom faces, as well as one of the

faces in the thickness direction, are fixed by zero normal-to-the-face displacements. The top face and the other face in the thickness direction are stress-free. A compressive Cauchy stress larger than the instability stress, but slightly below the corresponding Cauchy peak point, is prescribed on the left face. Due to the heterogeneously-distributed initial condition for the order parameter, the internal stresses are one order of magnitude smaller than the prescribed stress. However, they are sufficient to add up to the prescribed stress so that the local stress within some bulk zones slightly exceeds the Cauchy stress peak value.

Therefore, although the stresses throughout the sample are bellow the first Piola–Kirchhoff peak stress (i.e. strain is between two peak points), because at least one of the conditions for continuation of PT (in this case, for the Cauchy stress) is met, the PT evolves. During the PT, a martensitic band is formed and propagates until the stationary solution is reached. Interestingly, it is apparent that the complex internal stresses due to the large deformation of the boundary at the top region suppress the PT and prevent further movement of the interface.

In conclusion, the fulfillment of at least one of the conditions for PT completion suffices and there is no need to satisfy the conditions for all stress measures. This means that the chief stress measure, which is responsible for PT completion, is the measure with the lowest strain at the peak point. For the mentioned case in which PT is caused by compression, it was Cauchy stress; however, for the PT caused by tension, the chief stress measure would be the first Piola–Kirchhoff stress. Note that because the second Piola–Kirchhoff stress does not have its maximum in Fig. 1, when it is prescribed, the PT in a single element can be performed in a controlled way without mechanical instability.

5.2 Effect of stress hysteresis on PT

In a recent paper [49], the DFT simulations were employed to study the crystal lattice elastic instability during Si I $\leftrightarrow$ Si II PTs when subjected to a general stress tensor. For Si I $\rightarrow$ Si II PT, the instability stresses obtained by DFT simulations had excellent agreement with instability stresses from MD simulations [36,37]. However, for Si II $\rightarrow$ Si I PT, the instability stresses obtained by DFT were far below the MD results, producing a higher hysteresis. To study the effect of different instability stresses for the reverse PT, which in turn changes the stress hysteresis in the local stress–strain curves, on the nanostructure evolution, we considered different parallel reverse instability lines, shown in Fig. 4, using different calibration constants.

These lines are characterized by the instability stress at $\sigma_1 = \sigma_2 = 0$. We keep the same instability line for the direct PT ($\sigma_d = 12.29 \, \text{GPa}$) and consider four parallel lines for reverse PT, from $\sigma_r = 9.45 \, \text{GPa}$ obtained from the MD cali-
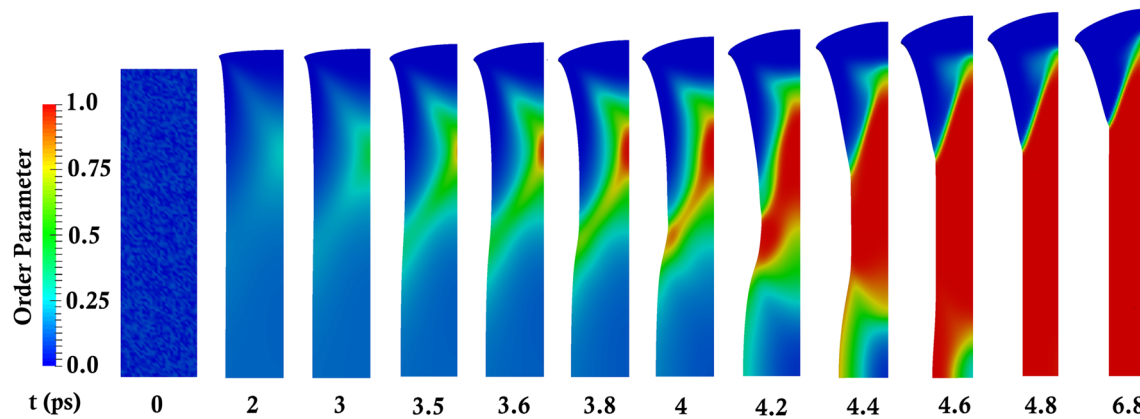
Fig. 3 Nanostructure evolution for prescribing compressive Cauchy stress at the left face with the magnitude slightly below the Cauchy stress peak point but above the instability stress

bration down to $\sigma_r = -3$ GPa for comparison. A 3D sample with the size $80 \times 80 \times 5$ nm is considered in this section. The periodic condition for both solution variables, namely the order parameter and displacement, is considered for the pair lateral right and left faces (orthogonal to the axis 1), as well as the top and bottom faces (orthogonal to the axis 3). One of the faces in the thickness direction (normal to the axis 2) is fixed for the normal-to-the-face displacement, namely $u_2 = 0$, and stress-free for shear stresses; it acts as the symmetry plane. The other face is stress-free. A relative compressive displacement u_3 is applied on the top and bottom faces and a tensile relative displacement u_1, proportional to the Poisson effect ($u_1 = \nu u_3$), is applied on the left and right pair faces. One displacement degree of freedom in directions 1 and 3 is required to be fixed, which was done at the center of the sample. To accelerate the martensitic band formation process, the initial condition for the order parameter is considered to be 0.1 within two inclined bands connecting the center of the external top and left faces, as well as the bottom and right faces. The initial order parameter is considered 0.01 anywhere else outside of the bands. It is worth mentioning that, if a randomly distributed initial value was considered, through quasi-static loading we would finally obtain such martensitic bands within the sample; however, this would increase the number of time steps and computation time by more than one order of magnitude.

The nanostructure evolution for three different cases of reverse instability lines are shown in Fig. 5. It can be observed that for the minimum hysteresis case (i.e. $\sigma_r = 9.45$ GPa), in addition to the formation of martensitic bands and their subsequent propagation, there is a homogeneous PT outside of the martensitic bands, which leads to an intermediate phase. However, as the hysteresis increases by shifting the reverse instability line down, the rate of homogeneous PT outside of the martensitic bands decreases such that, for the highest hysteresis case, PT is completed merely by propagation of
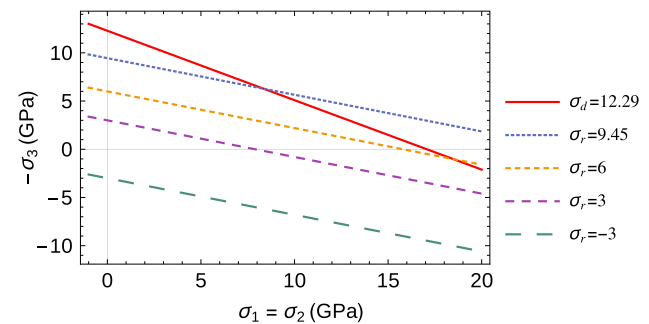

Fig. 4 Instability lines for direct PT and four different instability lines for reverse PT used for studying the effect of stress hysteresis on nanostructure evolution

the martensitic bands. The order parameter fields at $t = 2$ ps along a line passing through the bands from the upper right corner to the lower left corner are shown in Fig. 6. The vertical lines determine the width of one of the interfaces and half of the either martensitic or austenitic bands for the intermediate hysteresis case ($\sigma_r = 6$ GPa). It can be seen that the higher hysteresis not only leads to thinner interfaces and wider martensitic bands, but also decreases the value of the order parameter within the austenitic regions. The reason for such a nanostructure evolution can be further analyzed by considering the driving force field, which is shown in Fig. 7. It can be observed that, by increasing the hysteresis, the magnitude of the driving force increases within the interface and decreases outside of the interface, which can explain why the propagation of martensitic bands dominates the PT process for larger hysteresis.

Let us consider the effect of change in the hysteresis and the resultant nanostructure evolution on the internal stress fields. For this purpose, we study three different normal stress fields, namely normal-to-the-interface stress-σ_n, tangential-to-the-interface stress-σ_t and stress in the thickness direction-σ_2. These three stress fields are shown for the

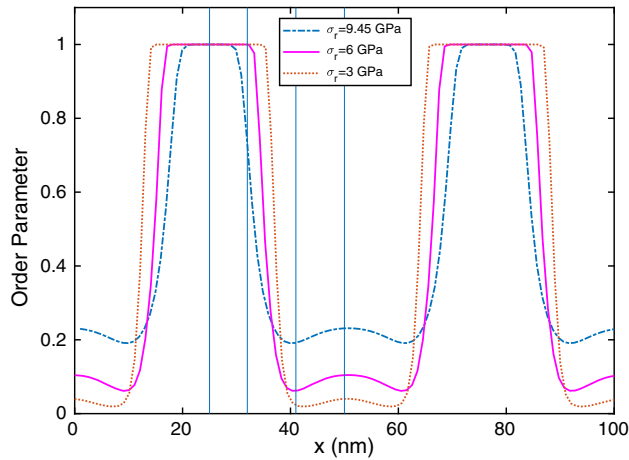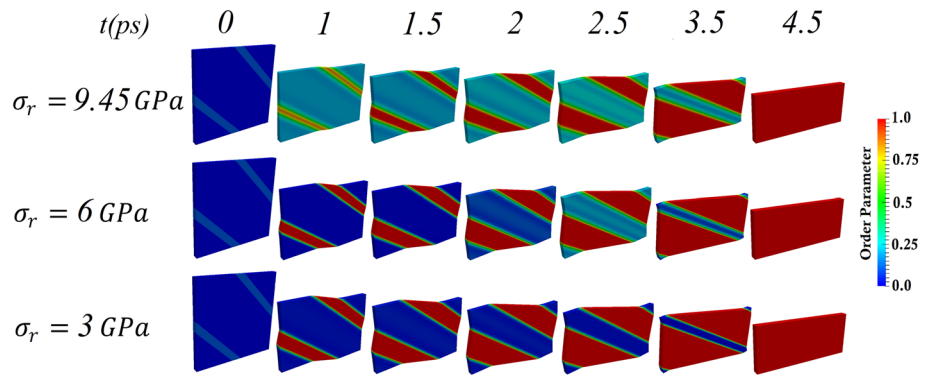**Fig. 5** Nanostructure evolution for three different reverse instability lines

Fig. 6 Distribution of the order parameter η at $t = 2$ ps along a line on the front face passing through the nanostructure from the upper right corner to the lower left corner for three different reverse instability lines
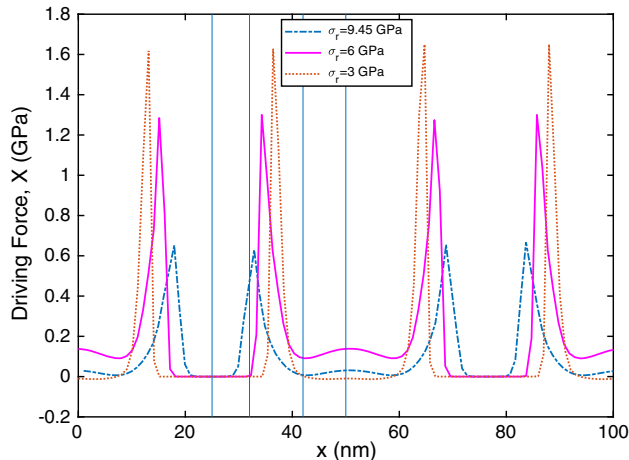

Fig. 7 Distribution of the driving force X at $t = 2$ ps along a line on the front face passing through the nanostructure from the upper right corner to the lower left corner for three different reverse instability lines

intermediate hysteresis case ($\sigma_r = 6$ GPa) at $t = 2$ ps in Fig. 8. They are also shown for all hysteresis cases along the previously-mentioned line passing through the bands in Figs. 9, 10 and 11. A number of remarks can be made based on Fig. 9. First, the overall compressive σ_n is higher within the martensitic bands than that within the austenitic bands. Second, the maximum and minimum stresses are both in the close vicinity of the interface such that the maximum stress is at the martensitic side of the interface and the minimum stress is at the austenitic side of the interface. Therefore, a sharp change in σ_n is observed within the interface. Third, by moving away from the interface, σ_n increases within the austenitic bands, whereas it decreases within the martensitic bands. Fourth, although increasing the hysteresis and consequently reducing the interface width leads to a decrease in overall σ_n, the difference between the maximum and minimum stress, specifically the change of stress within the interface, increases.

Next, some points can be noticed in Fig. 10 for the tangential-to-the-interface stress, σ_t. First, it is apparent that the compressive σ_t is at its minimum at the center of the martensitic bands and continues to increase toward the austenitic region where it reaches its maximum. However, there is a local minimum within the interface due to tensile interfacial stress. Second, although the increase in hysteresis does not significantly affect the σ_t within the martensitic region, it leads to a sharper increase within the interface and consequently higher values of σ_t within the austenitic regions.

Moreover, the normal stress in the thickness direction σ_2, is worth discussing. It should be noticed that the stress in the thickness direction is mostly produced by transformational extension within the martensitic bands. Therefore, σ_2 is highly concentrated at the interface where the interaction between expanding martensitic bands and resisting austenitic bands leads to a huge interfacial stress at the interface. This interfacial stress is compressive at the martensitic side, tensile at the austenitic side and tends to zero as it moves away from the interface. It can also be noticed that the increase in hysteresis, which leads to the thinner interfaces, in turn causes an increase in this stress.

Note that for the sharp interface, σ_n should be continuous across an interface. The large variation of σ_n across an interface in Fig. 9 is caused by its finite width, which is com-
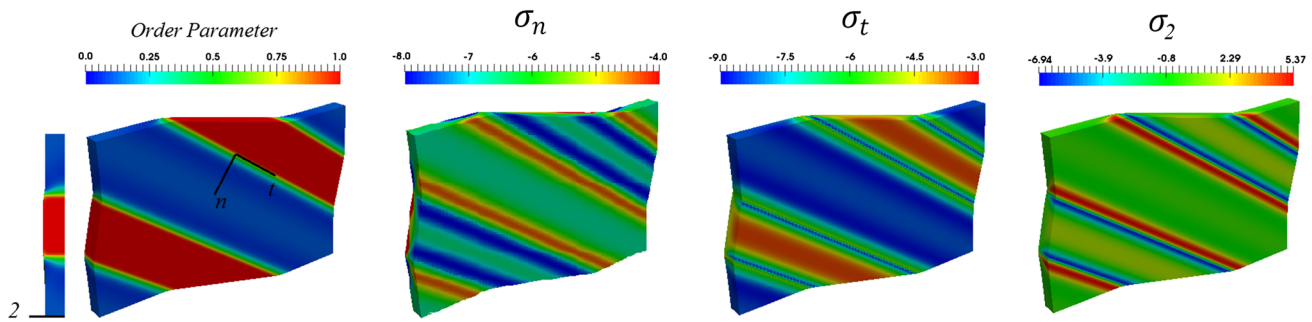
Fig. 8 Three different stress fields including normal-to-the-interface stress, tangential-to-the-interface stress and normal stress in the thickness direction for intermediate hysteresis case ($\sigma_r = 6$ GPa) at $t = 2$ ps
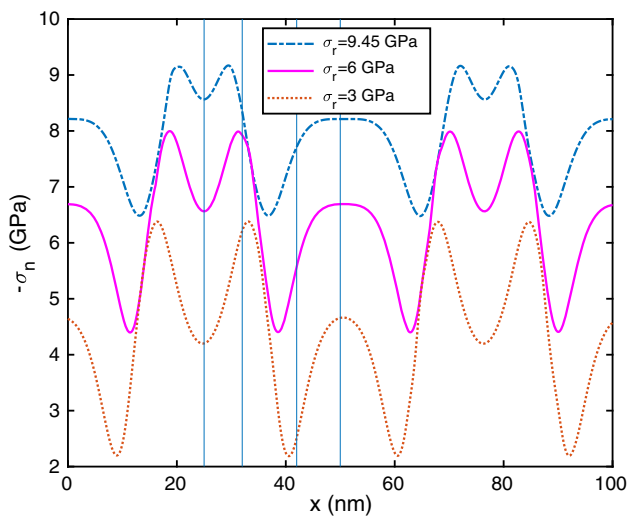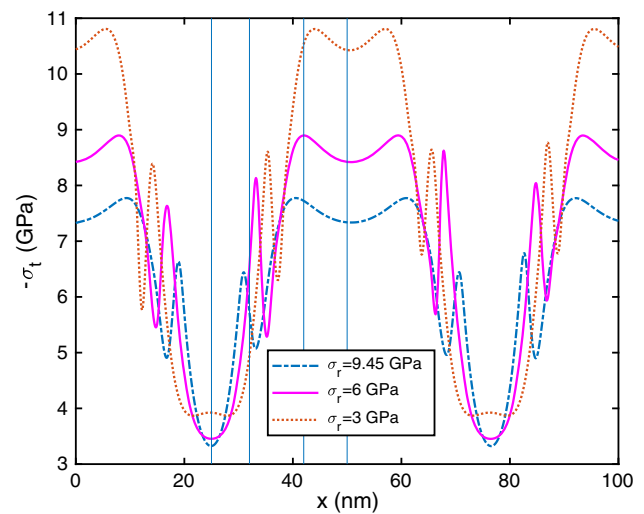

Fig. 9 Distribution of the normal-to-the-interface stress σ_n along a line on the front face passing through the nanostructure from the upper right corner to the lower left corner $t = 2$ ps for three different reverse instability lines

Fig. 10 Distribution of the tangential-to-the-interface stress, σ_t, along a line on the front face passing through the nanostructure from the upper right corner to the lower left corner $t = 2$ ps for three different reverse instability lines

parable with the thickness of a sample, the variable length of the interface, and variation of the stresses and the order parameter along the thickness of a sample.

5.3 Effect of stress in thickness direction on PT

In this section, the effect of the normal component of the stress tensor in the thickness direction σ_2 on nanostructure evolution is studied. The size of the sample, the boundary condition for the left and right pair faces, and the top and bottom pair faces, the initial condition for the order parameter, and the loading condition are the same as in the previous section. However, two different boundary conditions for the front and back faces (orthogonal to the direction 2) are considered. First, as in previous case studies, the back face is fixed for normal-to-the-face displacement and stress-free for shear stresses; the front face is stress-free. This means that, we are modeling the symmetric half of a sample twice as
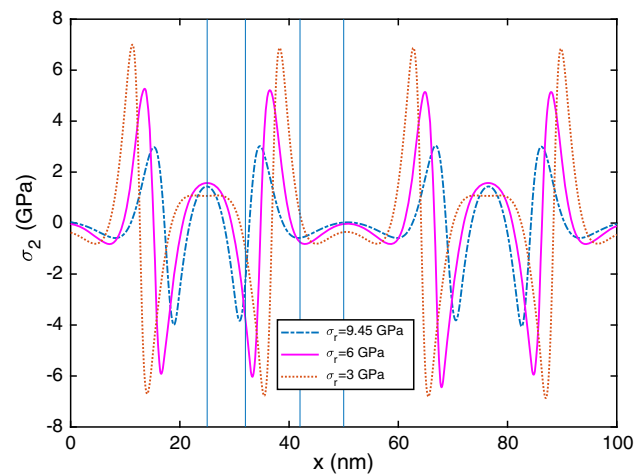

Fig. 11 Distribution of the normal-to-the-front-face stress, σ_2, along a line on the front face passing through the nanostructure from the upper right corner to the lower left corner $t = 2$ ps for three different reverse instability lines

Fig. 12 Nanostructure evolution for two different boundary conditions in the thickness direction: **a** periodic BC and **b** stress-free BC
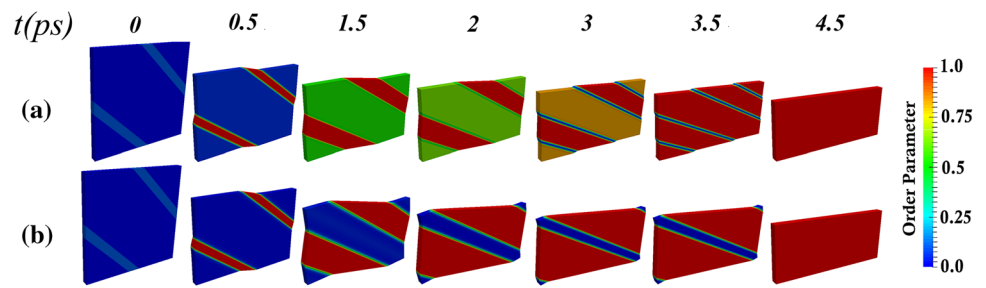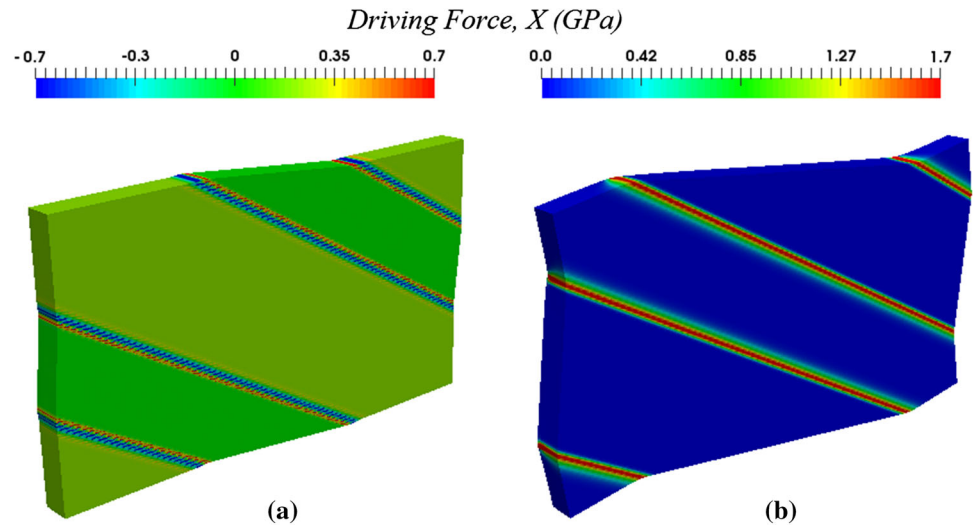

Fig. 13 Driving force for two different boundary conditions in the thickness direction: **a** periodic BC and **b** stress-free BC

thick with two free faces in the thickness direction. Second, we consider the periodic condition on a pair of front and back faces for both the order parameter and the displacement field. When applying periodicity, the relative tensile displacement between faces is prescribed at every time step, which is applied proportionally to the Poisson effect resulting from compressive displacement applied in the vertical direction, specifically $u_2 = \nu u_3$. It should be noticed that the reverse instability lines for both boundary condition cases are identical ($\sigma_r = 3\,\text{GPa}$).

The order parameter fields are shown in Fig. 12. For a stress-free boundary in the thickness direction, the PT is completed by the formation and propagation of martensitic bands. For periodic BC, although the martensitic bands are formed and widen to some extent, they stop propagating at some stage. Instead, the PT is completed by the instability and subsequent homogeneous transformation within the austenitic regions. This phenomenon can be described further by considering the field of driving force, and its value along a line passing through the bands at $t = 2\,\text{ps}$, shown in Figs. 13 and 14. It can be observed that, for stress-free conditions in the thickness direction, the driving force is non-negative everywhere, zero in the Si I bands, and localizes at the interface with a maximum value much larger than that for the periodic BC in the thickness direction. However, for periodic BC, there is a uniform positive driving force within the austenitic

region, and although the driving force reaches a maximum positive value within the interface at the martensitic side, it drops sharply to a negative minimum value at the austenitic side. Therefore, these ups and downs of driving force within the interface cancel each other and stop martensitic band broadening.

Such a difference in the nanostructure evolution and the driving force field can be explained by the field of the normal stress in the thickness direction σ_2 (Fig. 15). For stress-free BC, $\sigma_2 \simeq 0$ within the bulk phases and is only localized and oscillates within the interfaces. However, for periodic BC there is a restrictive compressive stress in the thickness direction against transformational expansion, because the transformation displacement exceeds the applied displacement on the external faces. Therefore, this huge compressive stress within the martensitic bands suppresses the propagation of the bands; compressive σ_2 in the austenite is much smaller, which promotes the homogeneous growth of the order parameter within the austenitic regions.

In the previous section, it was demonstrated that reducing the stress hysteresis leads to a homogeneous PT outside of the martensitic bands to some intermediate phases but increasing the stress hysteresis leads to growth of martensitic bands within austenite. Besides, it was explained in the current section that a restrictive periodic BC may lead to a complete homogeneous PT outside of martensitic bands. Here, these
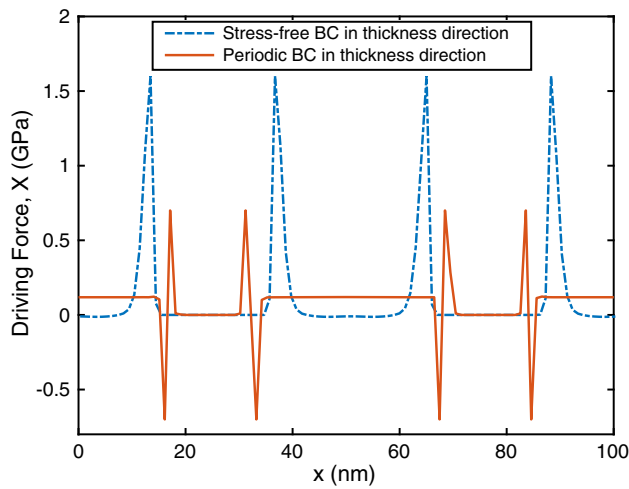
Fig. 14 Driving force along a line on the front face passing through the bands for two different boundary conditions in the thickness direction, namely for periodic BC and stress-free BC

two effects, specifically the effects of the hysteresis and of BC, are combined. Thus, we consider periodic BC in the thickness direction and increase the hysteresis by shifting the reverse instability line by 6 GPa down to $\sigma_r = -3$ GPa. It can be observed in Fig. 16 that the homogeneous PT outside of the martensitic bands converts into a mixture of two complete phases forming martensitic plates almost orthogonal to

two initial plates. Reverse PT in some regions of the primary martensitic plates reorients the structure, making the new plates the primary plates. At the next stage, in the austenitic region between the new plates, smaller-scale crossing plates form, repeating the previous plate-crossing process at smaller scale. If we were to treat a much larger sample, we would expect repetition of such a plate-crossing process at smaller and smaller scales, producing a fractal microstructure reminiscent of one observed experimentally in [13].

6 Conclusion

This paper is focused on an advanced PFA for stress-induced martensitic PTs which accounts for the crystal lattice instability conditions obtained by atomistic simulations. The numerical algorithm to solve the coupled phase field and mechanics equations was developed. The most general case of finite elastic and transformational strains was considered, and the anisotropic different elastic properties of phases were considered. As the previous PFA theories could not reproduce the lattice instability conditions obtained by atomistic simulations, new requirements were introduced for the thermodynamic potentials. The crystal lattice instability conditions for Si I ↔ Si II under multiaxial loading obtained by MD sim-

Fig. 15 Normal stress in the thickness direction, σ_2, for two different boundary conditions in thickness direction: **a** Stress-free BC and **b** Periodic BC
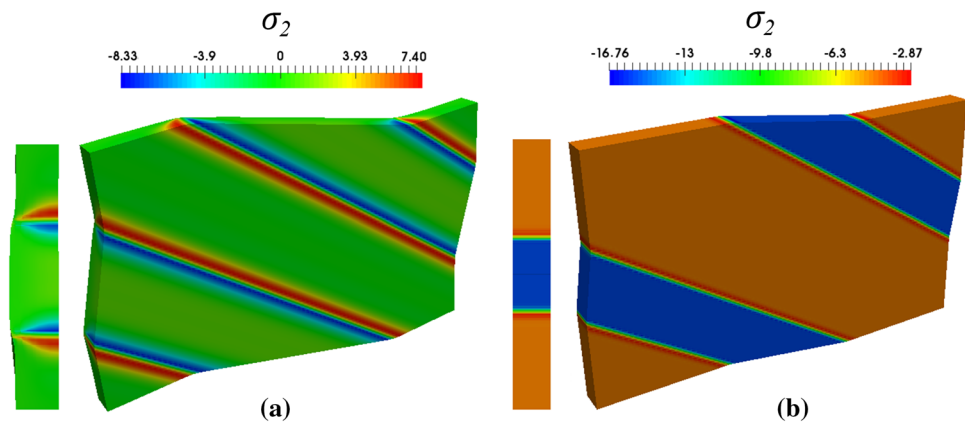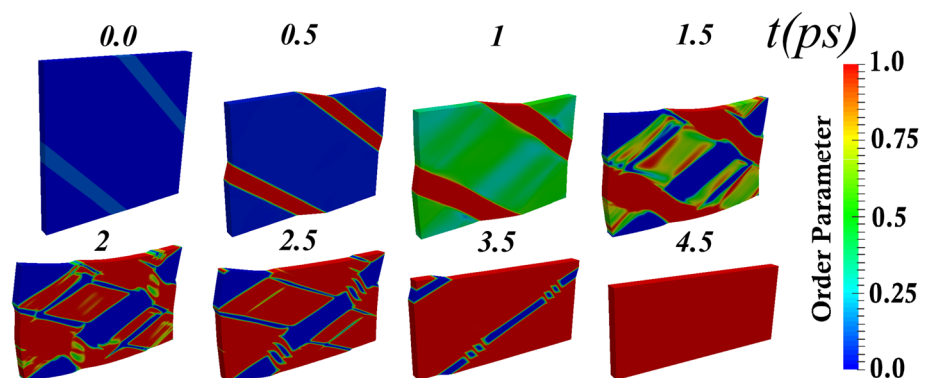

Fig. 16 Nanostructure evolution for reverse instability line $\sigma_r = -3$ GPa for periodic condition in the thickness direction

ulations in [36,37] was used to advance the PFA instability criteria. To reproduce the MD instability conditions,

– fifth degree polynomial interpolation functions of the order parameter are used;
– each independent component of the transformation strain tensor has different interpolation function parameters;
– interpolation functions for the elastic moduli should have zero second derivatives for the parent and product phases.

Finite element code has been developed in the deal.II program [3], a C++ library aimed at the computational solution of partial differential equations. Numerical solutions demonstrated that, on one hand, the initiation of the PT is independent of which stress measure is prescribed; on the other hand, however, the PT will not be completed unless the stress exceeds the stress peak point, which obviously depends on the prescribed stress measure. In addition, the relationship between increase in the distance between the direct and reverse instability stresses or stress hysteresis and the appearance of intermediate phases between martensitic bands was studied. Moreover, the effects of different boundary conditions, which cause different stress fields within the interfaces and bulks, on the mechanisms of nanostructure evolution were discussed.

Appendix

A: Derivation of the weak form of the mechanical equilibrium equation and linearization

In Sect. 3, we outline the weak forms for the mechanical equilibrium equations without details. We present the detailed derivation in this appendix. As described in Sect. 3, we have used a non-monolithic scheme to solve the governing equations, i.e. for solving for the displacements, we assume that the order parameter is constant in all iterations.

The weak form of the equilibrium equation (Eq. 13) is given by Eq. (39). Integrating Eq. (39) by parts and using the Gauss divergence theorem, the weak form is rewritten and can be presented as

$$R(\boldsymbol{u}, \delta\boldsymbol{u}) = \int_{\Omega_0} \boldsymbol{P}^T : \nabla_0 \delta\boldsymbol{u} \, dV_0 - \int_{S_{0T}} \bar{\boldsymbol{p}} \cdot \delta\boldsymbol{u} \, dS_0 = 0 \quad (74)$$

where we have used the identity $\nabla_0 \cdot (\boldsymbol{P}^T \cdot \delta\boldsymbol{u}) = (\nabla_0 \cdot \boldsymbol{P}) \cdot \delta\boldsymbol{u} + \boldsymbol{P}^T : \nabla_0 \delta\boldsymbol{u}$ and recall that $\bar{\boldsymbol{p}}$ is the specified traction on the traction boundary S_{0T}. Noticing that

$$\boldsymbol{E} = \frac{1}{2}(\boldsymbol{F}^T.\boldsymbol{F} - \boldsymbol{I}), \quad \delta\boldsymbol{F} = \nabla_0 \delta\boldsymbol{u} \quad \text{and}$$
$$\nabla_0(.) = \nabla(.).\boldsymbol{F} \quad (75)$$

the variation of the Lagrangian strain is expressed as

$$\delta\boldsymbol{E} = \frac{1}{2}(\nabla_0 \delta\boldsymbol{u}^T \cdot \boldsymbol{F} + \boldsymbol{F}^T \cdot \nabla_0 \delta\boldsymbol{u})$$
$$= \frac{1}{2}\boldsymbol{F}^T \cdot (\nabla\delta\boldsymbol{u}^T + \nabla\delta\boldsymbol{u}) \cdot \boldsymbol{F} = \boldsymbol{F}^T \cdot \delta\boldsymbol{\varepsilon} \cdot \boldsymbol{F} \quad (76)$$

with $\delta\boldsymbol{\varepsilon}$ given by Eq. (41). Utilizing the relations between the Piola–Kirchhoff and Cauchy stresses given by Eqs. (10) and (11), as well as using Eq. (76), the first integrand in Eq. (74) can be rewritten as

$$\boldsymbol{P} : \nabla_0(\delta\boldsymbol{u}) = \boldsymbol{S} : \boldsymbol{F}^T \cdot \nabla(\delta\boldsymbol{u}) \cdot \boldsymbol{F} = \boldsymbol{S} : \delta\boldsymbol{E} = \boldsymbol{\tau} : \delta\boldsymbol{\varepsilon}, \quad (77)$$

where $\boldsymbol{\tau} = J\boldsymbol{\sigma}$ is the Kirchhoff stress. Therefore, the weak form of the equilibrium equation Eq. (74) can be written in the form given by Eq. (40).

Because we will use the Newton's iteration for computing the displacements, we must linearize the weak form given by Eq. (40). In doing so we expand the weak form in a Taylor series about $\boldsymbol{u}$

$$R(\boldsymbol{u} + \Delta\boldsymbol{u}, \delta\boldsymbol{u}) = R(\boldsymbol{u}, \delta\boldsymbol{u})$$
$$+ \Delta R(\boldsymbol{u}, \Delta\boldsymbol{u}, \delta\boldsymbol{u}) + o(\Delta\boldsymbol{u}) = 0, \quad (78)$$

where $\Delta\boldsymbol{u}$ is an increment of the displacement vector, $\delta\boldsymbol{u}$ has been kept fixed, $o(\Delta\boldsymbol{u})$ consists of the higher order terms in $\Delta\boldsymbol{u}$ such that $\lim_{\Delta\boldsymbol{u}\to\boldsymbol{0}} o(\Delta\boldsymbol{u})/|\Delta\boldsymbol{u}| = 0$, and $\Delta R(\boldsymbol{u}, \Delta\boldsymbol{u}, \delta\boldsymbol{u})$ is the directional derivative of R defined as [48]

$$\Delta F(\boldsymbol{u}, \Delta\boldsymbol{u}, \delta\boldsymbol{u}) = DF(\boldsymbol{u}, \delta\boldsymbol{u}) \cdot \Delta\boldsymbol{u}$$
$$= \frac{d}{d\epsilon}F(\boldsymbol{u} + \epsilon\Delta\boldsymbol{u}, \delta\boldsymbol{u})\bigg|_{\epsilon=0} \quad (79)$$

for any differentiable functional or function F.

The linearized form of residual R in Eq. (40) can be expressed as

$$DR \cdot \Delta\boldsymbol{u} = \int_{\Omega_0} \Delta\boldsymbol{S} : \delta\boldsymbol{E} \, dV_0 + \int_{\Omega_0} \boldsymbol{S} : \Delta(\delta\boldsymbol{E}) \, dV_0. \quad (80)$$

We will now derive an amenable form of the integrands in Eq. (80).

Noticing that U_t is independent of u, we derive the expression for the increment of S using Eq. (11):

$$\Delta S = J_t U_t^{-1} \cdot \Delta \hat{S} \cdot U_t^{-1} = J_t U_t^{-1} \cdot (C : \Delta E_e) \cdot U_t^{-1}, \tag{81}$$

where C is the fourth order elastic modulus tensor with respect to Ω_t and is given by Eqs. (27) and (44). Using Eq. (3)$_1$, we show that the increments ΔE_e and ΔE are related by

$$\Delta E_e = U_t^{-1} \cdot \Delta E \cdot U_t^{-1}, \tag{82}$$

which we use to rewrite Eq. (81) as

$$\begin{aligned} \Delta S &= J_t U_t^{-1} \cdot (C : U_t^{-1} \cdot \Delta E \cdot U_t^{-1}) \cdot U_t^{-1} \\ &= \mathcal{C} : \Delta E, \end{aligned} \tag{83}$$

where $\mathcal{C}$ is the fourth order elasticity tensor defined in the reference configuration Ω_0, which is related to C by

$$\mathcal{C}^{IJKL} = J_t (F_t^{-1})^{Ii} (F_t^{-1})^{Jj} (F_t^{-1})^{Kk} (F_t^{-1})^{Ll} C^{ijkl}. \tag{84}$$

Note that the indices in upper case, i.e. I, J, etc. are for Ω_0 and the indices in lower case, i.e. i, j, etc., are for Ω_t. Using Eqs. (76) and (83), we rewrite the first integrand of Eq. (80) as

$$\begin{aligned} \Delta S : \delta E &= \delta E : \mathcal{C} : \Delta E \\ &= F^T \cdot \delta \varepsilon \cdot F : (\mathcal{C} : F^T \cdot \Delta \varepsilon \cdot F) \\ &= \delta \varepsilon : J \mathsf{C} : \Delta \varepsilon, \end{aligned} \tag{85}$$

where we have used (see Chapter 10 of [51])

$$\Delta E = F^T \cdot \Delta \varepsilon \cdot F, \tag{86}$$

with $\Delta \varepsilon$ given by Eq. (45) and C as the fourth order elasticity tensor defined in Ω, which is given by Eq. (43).

Next, let us simplify the second integrand in Eq. (80). It can be obtained from Eq. (76) that

$$\begin{aligned} \Delta(\delta E) &= \frac{1}{2}(\nabla_0 \Delta u^T \cdot \nabla_0 \delta u + \nabla_0 \delta u^T \cdot \nabla_0 \Delta u) \\ &= \frac{1}{2} F^T \cdot (\nabla \Delta u^T \cdot \nabla \delta u + \nabla \delta u^T \cdot \nabla \Delta u) \cdot F. \end{aligned} \tag{87}$$

Thus, noticing that $S = F^{-1} \cdot \tau \cdot F^{-T}$, the second integrand of Eq. (80) is expressed as

$$S : \Delta(\delta E) = \nabla \delta u : \tau \cdot \nabla \Delta u^T. \tag{88}$$

Therefore, Eq. (80) simplifies to the form given by Eq. (42).

References

1. Artemev A, Jin YM, Khachaturyan AG (2001) Three-dimensional phase field model of proper martensitic transformation. Acta Mater 49:1165–1177
2. Babaei H, Levitas VI (2018) Phase field approach for stress- and temperature-induced phase transformations that satisfies lattice instability conditions. Part 2: simulations for phase transformations Si I↔Si II. Int J Plast 107:223–245
3. Bangerth W, Hartmann R, Kanschat G (2007) Deal. II—a general purpose object oriented finite element library. ACM Trans Math Softw 33(4):1–27
4. Barsch GR, Krumhansl JA (1984) Twin boundaries in ferroelastic media without interface dislocations. Phys Rev Lett 53:1069–1072
5. Blank VD, Estrin EI (2014) Phase transitions in solids under high pressure. CRC Press, Boca Raton
6. Chen LQ (2002) Phase-field models for microstructure evolution. Annu Rev Mater Res 32:113–140
7. Falk F (1983) Ginzburg–Landau theory of static domain walls in shape-memory alloys. Z Physik B Condens Matter 51:177–185
8. Finel A, Le Bouar Y, Gaubert A, Salman U (2010) Phase field methods: microstructures, mechanical properties, and complexity. C R Phys 11:245–256
9. Domnich V, Gogotsi Y (2004) Indentation-induce phase transformations in ceramics. In: Gogotsi Y, Domnich V (eds) High pressure surface science and engineering. Institute of Physics, Bristol and Philadelphia, pp 443–466
10. He Y, Zhong L, Fan F, Wang C, Zhu T, Mao SX (2016) In situ observation of shear-driven amorphization in silicon crystals. Nat Nanotechnol 11(10):866
11. Hennig RG, Wadehra A, Driver KP, Parker WD, Umrigar CJ, Wilkins JW (2010) Phase transformation in Si from semiconducting diamond to metallic beta-Sn phase in QMC and DFT under hydrostatic and anisotropic stress. Phys Rev B 82:014101
12. Hill R, Milstein F (1977) Principles of stability analysis of ideal crystals. Phys Rev B 15:3087–3096
13. Hornbogen E (1998) Legierungen mit Formgedächtnis. Rheinisch–Westfälische Akademie der Wissenschaften, Vorträge 388
14. Jacobs AE (1992) Finite-strain solitons of a ferroelastic transformation in two dimensions. Phys Rev B 46:8080–8088
15. Javanbakht M, Levitas VI (2016) Phase field simulations of plastic strain-induced phase transformations under high pressure and large shear. Phys Rev B 94:214104
16. Javanbakht M, Levitas VI (2018) Nanoscale mechanisms for high-pressure mechanochemistry: a phase field study. J Mater Sci 53:13343–13363
17. Ji C, Levitas VI, Zhu H, Chaudhuri J, Marathe A, Ma Y (2012) Shear-induced phase transition of nanocrystalline hexagonal boron nitride to wurtzitic structure at room temperature and lower pressure. Proc Natl Acad Sci USA 109:19108–19112
18. Jin YM, Artemev A, Khachaturyan AG (2001a) Three-dimensional phase field model of low-symmetry martensitic transformation in polycrystal: simulation of ζ_2 martensite in AuCd alloys. Acta Mater 49:2309–2320
19. Lekhnitskii SG (1963) Theory of elasticity of an anisotropic elastic body. Holden-Day Inc, Toronto
20. Levitas VI (2004) Continuum mechanical fundamentals of mechanochemistry. In: Gogotsi Y, Domnich V (eds) High pressure surface science and engineering. Institute of Physics, Bristol, pp 159–292 (Section 3)
21. Levitas VI (2004a) High-pressure mechanochemistry: conceptual multiscale theory and interpretation of experiments. Phys Rev B 70:184118
22. Levitas VI (2013) Phase-field theory for martensitic phase transformations at large strains. Int J Plast 49:85–118

23. Levitas VI (2013b) Thermodynamically consistent phase field approach to phase transformations with interface stresses. Acta Mater 61:4305–4319

24. Levitas VI (2013c) Interface stress for nonequilibrium microstructures in the phase field approach: exact analytical results. Phys Rev B 87:054112

25. Levitas VI (2014) Unambiguous Gibbs dividing surface for nonequilibrium finite-width interface: static equivalence approach. Phys Rev B 89:094107

26. Levitas VI (2014a) Phase field approach to martensitic phase transformations with large strains and interface stresses. J Mech Phys Solids 70(2014):154–189

27. Levitas VI (2018) Phase field approach for stress- and temperature-induced phase transformations that satisfies lattice instability conditions. Part I. General theory. Int J Plast 106:164–185

28. Levitas VI, Javanbakht M (2010) Surface tension and energy in multivariant martensitic transformations: phase-field theory, simulations, and model of coherent interface. Phys Rev Lett 105:165701

29. Levitas VI, Javanbakht M (2014) Phase transformations in nanograin materials under high pressure and plastic shear: nanoscale mechanisms. Nanoscale 6:162–166

30. Levitas VI, Preston DL (2002a) Three-dimensional Landau theory for multivariant stress-induced martensitic phase transformations. I. Austenite ↔ Martensite. Phys Rev B 66:134206

31. Levitas VI, Preston DL (2002b) Three-dimensional Landau theory for multivariant stress-induced martensitic phase transformations. II. Multivariant phase transformations and stress-space analysis. Phys Rev B 66:134207

32. Levitas VI, Shvedov LK (2002) Low pressure phase transformation from rhombohedral to cubic BN: experiemnt and theory. Phys Rev B 65(10):104109(1–6)

33. Levitas VI, Warren JA (2016) Phase field approach with anisotropic interface energy and interface stresses: large strain formulation. J Mech Phys Solids 91:94–125

34. Levitas VI, Preston DL, Lee DW (2003) Three-dimensional Landau theory for multivariant stress-induced martensitic phase transformations. III. Alternative potentials, critical nuclei, kink solutions, and dislocation theory. Phys Rev B 68:134201

35. Levitas VI, Levin VA, Zingerman KM, Freiman EI (2009) Displacive phase transitions at large strains: phase-field theory and simulations. Phys Rev Lett 103:025702

36. Levitas VI, Chen H, Xiong L (2017a) Triaxial-stress-induced homogeneous hysteresis-free first-order phase transformations with stable intermediate phases. Phys Rev Lett 118:025701

37. Levitas VI, Chen H, Xiong L (2017b) Lattice instability during phase transformations under multiaxial stress: modified transformation work criterion. Phys Rev B 96:054118

38. Mamivand M, Zaeem MA, el Kadiri H (2013) A review on phase field modeling of martensitic phase transformation. Comput Mater Sci 77:304–311

39. Milstein F, Marschall J, Fang H (1995) Theoretical bcc–fcc transitions in metals via bifurcations under uniaxial load. Phys Rev Lett 74:2977–2980

40. Olson GB, Cohen M (1972) A mechanism for the strain-induced nucleation of martensitic transformation. J Less Common Met 28:107

41. Olson GB, Cohen M (1986) Dislocation theory of martensitic transformations. In: Nabarro FRN (ed) Dislocations in solids, vol 7. Elsevier Science Publishers B V, New York, pp 297–407

42. Olson GB, Roytburd AL (1995) Martensitic nucleation. In: Olson GB, Owen WS (eds) Martensite, Ch 9. The Materials Information Society, Russell Township, pp 149–174

43. Patten J (2004) Ductile regime machining of semiconductors and ceramics. In: Gogotsi Y, Domnich V (eds) High pressure surface science and engineering. Institute of Physics, Bristol and Philadelphia, p 543632

44. Vedantam S, Abeyaratne R (2005) A Helmholtz free-energy function for a Cu–Al–Ni shape memory alloy. Int J Non-Linear Mech 40:177–193

45. Wang Y, Khachaturyan AG (2006) Multi-scale phase field approach to martensitic transformations. Mater Sci Eng A 438:55–63

46. Wang J, Yip S, Phillpot SR, Wolf D (1993) Crystal instabilities at finite strain. Phys Rev Lett 71:4182–4185

47. Wasmer K, Wermelinger T, Bidiville A, Spolenak R, Michler J (2008) In situ compression tests on micron-sized silicon pillars by Raman microscopy Stress measurements and deformation analysis. J Mater Res 23(11):3040–3047

48. Wriggers P (2008) Nonlinear finite element methods. Springer, Heidelberg

49. Zarkevich NA, Chen H, Levitas VI, Johnson DD (2018) Lattice instability during solid-solid structural transformations under a general applied stress tensor: example of Si I Si II with metallization. Phys Rev Lett 121(16):165701

50. Zhu J, Wu H, Wang D, Gao Y, Wang H, Hao Y, Yang R, Zhang T, Wang Y (2017) Crystallographic analysis and phase field simulation of transformation plasticity in a multifunctional β-Ti alloy. Int J Plast 89:110–129

51. Zienkiewicz OC, Taylor RL (2000) The finite element method: volume 2- solid mechanics. Butterworth-Heinemann, Woburn